Heliyon 9 (2023) e18474

Contents lists available at ScienceDirect

Heliyon

journal homepage: www.cell.com/heliyon

Modeling and optimization of green-Al 6061 prepared from environmentally source materials

Adeolu Adesoji Adediran [a,d,*], Abayomi Adewale Akinwande [b,**], Olanrewaju S. Adesina [c], Victor Agbaso [a], Oluwatosin Abiodun Balogun [b], B. Ravi Kumar [d]

[a] Department of Mechanical Engineering, Landmark University, Omu-Aran, Kwara State, Nigeria
[b] Department of Metallurgical and Materials Engineering, Federal University of Technology, Akure, Ondo State, Nigeria
[c] Department of Mechanical Engineering, Redeemers University, Ede, Osun State, Nigeria
[d] MTE Division, CSIR-National Metallurgical Laboratory, Jamshedpur, India

ARTICLE INFO

Keywords:
Characterization
Mechanical properties
Al6061
Casting methods
Composites
Grains

ABSTRACT

Recent studies are evaluating the use of particulates fabricated from agro-based residues as reinforcement for enhancing the properties of aluminium alloys. This report focuses on the optimization approach and modeling of responses for future prediction, which are absent from the majority of studies involving particle reinforcement of an aluminum matrix. Herein, palm kernel shell ash (PKA) and rice husk ash (RHA) were incorporated with 4 wt% of WSD and used as fillers in the Aluminium-6061 matrix at variable proportions. The response surface approach was utilized in the experiment design, modeling, and outcome optimization. The independent variables are the proportions of PKA and RHA and stir casting temperature. Yield, ultimate tensile, impact strength, elastic modulus, and fracture toughness are examined as response parameters. The results demonstrated that the microstructural property played a significant role in the responses. Incorporating PKA and RHA into the Al-6061 matrix improved the response parameters. Temperatures in the range of 700 and 800 °C enhanced the property parameters, even though temperatures within 800 and 900 °C caused a decline in response. The dependence of the responses on the pattern between property variables was revealed by surface and contour plots. The development of models for predicting responses. Optimal conditions were reached at 4.03% PKA, 5.12% RHA, and 787 °C, with an error <5% when compared to the forecast responses, thus validating the model.

1. Introduction

Agriculture remains an inevitable aspect of human because of the relevance of food being the major need of man. In the last decade, agricultural activities have increased tremendously. Consequently, agro-wastes have also increased requiring more effort in disposing them [1,2]. In a way to reduce the load effect of these wastes on the environment, agro wastes are recycled, reduced, and reused. There are documented findings in the reuse of many agro wastes in metal, polymer, and ceramic composite production [3–5]. Waste products

* Corresponding author. Department of Mechanical Engineering, Landmark University, Omu-Aran, Kwara State, Nigeria.
** Corresponding author.
E-mail addresses: adediran.adeolu@lmu.edu.ng (A.A. Adediran), abypublications@gmail.com (A.A. Akinwande).

https://doi.org/10.1016/j.heliyon.2023.e18474
Received 30 March 2023; Received in revised form 18 July 2023; Accepted 19 July 2023
Available online 20 July 2023

have been reported to contribute significantly to improving the properties of developed composites [6]. In aluminum matrix composites (AMCs) production, agro waste particulate has gained attention as a substitute for synthesized ceramic additives like SiC, Al_2O_3, SiO_2, B_4C, WC, TiO_2, TiN, and TiC which are majorly imported in most developing countries. Some of these agro-based materials are reprocessed into powdery ash forms and employed in reinforcing aluminium base matrix as alternatives to the synthetic ceramic for the motive of cost reduction. These reinforcing materials include coconut shell ash [7,8], rice husk ash [1,9], palm kernel ash [10,11], bamboo leaf ash [12–14], eggshell [15], and others. From the survey of works of literature reported, it is evident that these materials when used as reinforcements contribute to microstructural modification thereby enhancing the property of AMCs under investigation.

Aluminium metal is highly sort after by manufacturers for several applications. This is due to its lightweight and relatively high strength, most lightweight and ductile applications are conceived with aluminium-based components being the major constituents of the design. In comparison with steel, aluminium is lighter but possesses lower strength. There is a growing interest among researchers to develop aluminium alloy composites to improve the properties of the base matrix. Hybrid reinforced composites are achieved by the combination of two or more reinforcements into an aluminium alloy matrix for a desirable property when compared with the monolithic alloy [16,17]. Studies have shown that agro-waste materials are viable as reinforcement materials due to the silica content in their network [1]. Authors [18] reported on the blend of boron carbide and coconut shell ash in an aluminium 7075 matrix design. Findings from Ref. [19] showed the viability of using the blend of eggshell powder and SiC in aluminium metal matrix production. Their findings show a similar result with [20] as aluminium matrices were improved by the hybrid reinforcements. In another report [6], achieved enhancement in the mechanical performance of aluminium alloy by the addition of two reinforcements, eggshell, and TiO_2. In another report [21], Talabi and his team introduced snail shell ash and waste glass powder in varying ratios in aluminium alloy with the consequence of improving the properties of the alloy. Our study involved primarily the addition of palm kernel shell (PKS) and rice husk ash (RSA) in varying combinations in Al-6061 as a way of developing hybrid aluminium composites. These materials are abundant within the locality of this research, hence the choice of using them as reinforcing materials. Also, this will serve as a way of reducing their environmental pollution when they are discarded, justifying their use in this study. The presence of silica phase in their structure makes these two agro wastes a potential material for reinforcement in aluminium composite production. The quest to contribute to knowledge on aluminium metal matrix composites develop by hybrid reinforced agro wastes and waste steel chips at constant dosage is the gap the present study attempt to fill. More so, there are scanty works of literature on response modeling of this set of hybrid reinforcements for future property predictions, the gap of which was addressed in this study.

Waste steel chips were added as supplementary reinforcement in fixed proportion to the hybrid reinforced materials. The use of waste steel chips is gradually gaining prominence as reinforcement in aluminium matrix [22]. Machining and milling operations for steel products are often followed by metal chips or swarf. These chips are often disposed on landfills. Unfortunately, these materials are hard to degrade and continuous discarding in landfills contributes to environmental degradation. In this study, metal chips (waste steel chips) realized from the machining process of medium carbon steel are gathered for the hybridization of Al 6061. Since metal chips are considered to possess ductility and toughness, metal chip waste is considered to be recycled into the aluminium melt to give a balance of the property.

Hence, the present paper reports on the use of palm kernel shell ash (PKA), rice husk ash (RHA), as well as steel chips (at a constant dose of 4 wt %) in Al 6061 towards observing the effect on the mechanical properties. For proper wettability, a pre-heat treatment of the reinforcements was done and the use of wetting agents was earlier reported by Ref. [23]. Similar to previous studies [16,24], response surface method was utilized in the composite combination, modeling of the property parameters, and derivation of optimization input parameters toward achieving balanced performance. The input variables are PKA powders, RHA proportion, and stirring temperature. Stirring temperature was chosen as the input variable because of the role of stirring temperature in the degree of dispersion of the particles which in a way affects the properties parameters of the developed composite.

2. Materials and methods

2.1. Materials preparation

The inputs used in this study are aluminium Al 6061 ingot, palm kernel shell, rice husk ash, and medium carbon steel chips. The aluminium ingot was obtained from Shanghai Worldyang Chemical Co. Ltd India). Palm kernel shells were locally sourced, they were washed to eliminate dirt and dried in open air for 24 h. Afterward, the outer shell was smashed into smaller particles and grinded into powder via a grinder and further pulverized into powder. This procedure was followed by heating in a laboratory furnace at 720 °C for 6 h. Afterward, the palm kernel ash and allowed to cool in the furnace. The process continued by breaking of the lumps into powder and further ball milling for 4 h. Palm kernel shell ash (PKA) sieved to −23 μm was collected for the experiment. Equally, the rice husk was collected, washed with water, and opened dried for 48 h. The dried husk was made to pass through the same stage like the palm kernel shell until the ash was sieved to 23 μm passing. Waste steel shavings obtained from the machining operation of medium carbon steel materials were collected, initially sieved to −300 μm, and milled via a ball mill. The waste steel powder was sieved to 75-μm passing was packed for the specimen preparation.

2.2. Design experimentation

2.2.1. Response surface method (RSM)

RSM entails a statistical and numerical approach for modeling a group of data [25]. RSM is employed in this study in the design of an experiment based on Box-Behnken design (BBD) as practiced [6,25]. BBD studies the effect of input factors and their interaction

with responses. More so, its acceptance for the design of experiments is based on the ability to obtain high order response surface via fewer experimental runs as compared with full factorial design, hence its less expensive [26]. The design engages 12 middle points and 3 center points to generate a fit regression model. The experimental variables or factors are PKA powders, RHA proportion, and stirring temperature, even as waste steel debris was held constant at 4 wt %. The dependent variables which are the responses are yield strength, ultimate tensile strength, fracture toughness, and impact strength. A second-degree polynomial model (equation (1)) was established for each response towards accessing the influence of the variable on the responses.

$$Y = a_0 + a_1N_1 + a_2N_2 + a_3N_3 + a_{12}N_1N_2 + a_{13}N_1N_3 + a_{23}N_2N_3 + a_{11}N_1^2 + a_{22}N_2^2 + a_{33}N_3^2 \quad (1)$$

The experimental inputs are N_1, N_2, and N_3 corresponding to PKA powders, RHA, and stirring temperature. Similarly, a_1, a_2, a_3, a_{12}, a_{13}, a_{23}, a_{11}, a_{22}, and a_{33}, are coefficient of model terms. Table 1 indicates levels of the experimental design for each independent variable while Table 2 shows the mix design for the experimental.

2.3. Composite development

Composite development involves the initial process of pre-heat treatment of the reinforcements in oven drying of the waste steel chips, PKA, and RHA particulate at 200 ± 5 °C for 12 h for proper wettability and to eliminate dampness following the protocol stated by Ref. [23]. 4 wt % fixed level of waste steel chips were combined with PKA and RHA according to combinations indicated by the experimental runs in Table 2. The aluminium ingot was charged into a graphite crucible initially heated to 520 °C. The temperature was increased to values indicated in Table 2 to achieve the molten metal of the ingot. After that, the particle mix (preheated to 500 °C) was introduced at 5 g/min for each experimental run. The mixture was stirred at 350 rpm for another 10 min. A sequel to this was the pouring of the liquid composite into metal moulds which allowed it to cool to room temperature.

2.4. Property evaluation

2.4.1. Mechanical properties

The tensile behavior of the specimens under loading was conducted on samples sectioned to 30 mm gauge length and 5 mm diameter. A universal testing machine (H001C) was used at a strain rate of 10^{-3}/s with a load of 50 kN according to standard protocol [27]. For repeatability of results, triplicate tests representing each composition were tested. Yield strength and ultimate tensile strength were estimated from the outcomes obtained. The fracture toughness of the samples was evaluated on triplicate samples through the procedure of circumferential notch tensile test on samples machined to 60 mm gauge length, 5.5 mm gauge diameter, and 4.5 mm notch diameter [23]. The notch tensile strength indicated as T_n in equation (2) was obtained from the load-displacement curve. The value for each sample was evaluated via equation (1).

$$K = 0.454 * d^{0.5} * T_n \quad (2)$$

The attainment for the plane strain was analyzed via equation (3). K stands for fracture toughness (MPa.$m^{0.5}$), d represent the gauge diameter (mm), and T_n the notched tensile strength (MPa). T_s stands for yield strength (MPa).

$$d \geq \left(\frac{K}{Ts}\right) \quad (3)$$

The Charpy impact strength was evaluated on triplicate samples (of dimension 55 × 10 × 10 mm^3) representing each experimental run according to Ref. [28], the samples were notched at 60 °using a JB-300B machine.

2.4.2. Microstructural and phases characterization

For the microstructural study, samples were sectioned, and the surface was ground and polished using different grades of emery paper/cloth. Etching was carried out by applying 0.5% hydrogen fluoride on the surface for 20 s via swabbing. The microstructure of the samples was assessed by the use of a scanning electron microscope (JSM 7900F) attached with Energy dispersive spectrometer (EDX) [29]. X-ray diffraction analysis (XRD) was employed for the phase identification by use of Bruker D2 Phaser XRD tester following the protocol reported by authors [30]. The samples were scanned in the 2θ range of 10–90° at scanning ratio of 2.5°/min.

2.4.3. Properties of matrix materials

The properties of the aluminium 6061 are 2.76 g/cc density, 83 HRB Brinell hardness, 454 MPa yield strength, 526 MPa ultimate tensile strength, 70.6 GPa elastic modulus, and 14.26 MPa $m^{0.5}$ fracture toughness.

The elemental composition depicted in Fig. 1 shows a high peak of Al as a major element while other elements such as Fe, Zn, Mg,

Table 1
Control variables and their levels.

Variables	Min (−1)	Middle (0)	Max (+1)
PKA	2	4	6
RHA	2	4	6
Stirring temperature	700	800	900

Table 2
Experimental design showing the experimental run, coded level and factors.

Experimental run	Coded levels			Factors		
	A	B	C	A (%)	B (%)	C (°C)
1	−1	0	1	2	4	900
2	0	1	1	4	6	900
3	1	1	0	6	6	800
4	−1	−1	0	2	2	800
5	1	0	1	6	4	900
6	0	1	−1	4	6	700
7	0	1	0	2	6	800
8	1	0	0	6	2	800
9	1	0	0	6	4	700
10	0	−1	−1	4	2	700
11	−1	0	−1	2	4	700
12	0	−1	1	4	2	900
13	0	0	0	4	4	800
14	0	0	0	4	4	800
15	0	0	0	4	4	800

Si, Cu, Mn, and Cr, are by the element composition. The compositions simply confirm that the alloy is typical of Al 6061 [31].

Table 3 reveals the chemical and elemental constituent of the input materials. It is evident in Table 3 that PKA has a silica phase with 20.15% of CaO while RHA showed the highest phase of silica. Other chemical compounds are MgO, Al_2O_3, Fe_2O_3, and others.

It is evident that the waste steel chips contain majorly iron as the base element as expected with the presence of alloying elements like Cu, C, P, Cr, Si, Mn, Ni, and S. The scanning electron microscope image of the input materials, PKA and RHA as well as the phases presented are presented in Fig. 2.

The elemental constituent of the steel particles used contain the following, Cu: 0.11, C: 0.33, P: 0.011, Cr: 0.08, Si: 0.24, Mn: 0.64, Ni: 0.08, Mo: 0.01, S: 0.064 and Fe balance.

Fig. 2a reveals the SEM micrographs for PKA and Fig. 2b RHA used in this study. The particles were randomly distributed in the structure. From the XRD result presented in Fig. 2c, silica is noted to be present in high quantity with diffraction peaks at 26.2°, 38.0°, 46.3°, and 54.8° as confirmed in the DB card number 01-082-1574. Calcite was also observed among the phases identified in the XRD with peak positions of 33.2°, 51.8°, 56.2° and 63.8° (DB card number: 01-085-6710), confirming the result presented from the elemental constituents. This trend was consistence with the result of authors [32] earlier reported in the literature. According to the phases identified for rice husk ash in Fig. 2c, SiO_2 is the dominant phase with a DB card number 01-082-1574 at 2θ values of 19.5, 24.7, 32.8, 37.6, 42.5, 47.1, and 50.1°. Similar findings were supported by Ref. [33] in their study. The result agrees with the data presented in Table 3 which indicated that SiO_2 in RHA showed an optimum silica value.

3. Results and discussion

3.1. Microstructural analysis

Fig. 4a–d and Fig. 5a–d presents the morphological features and EDX results obtained in the samples prepared at 700 and 800 °C. Fig. 4a and b displays the morphology of the samples containing with 2 wt % PKA/4 wt % RHA and 4 wt % PKA/2 wt % RHA and cast at 700 °C.

It was noted that the reinforcing particles are disseminated in the matrix. The presence of steel debris was evident in the

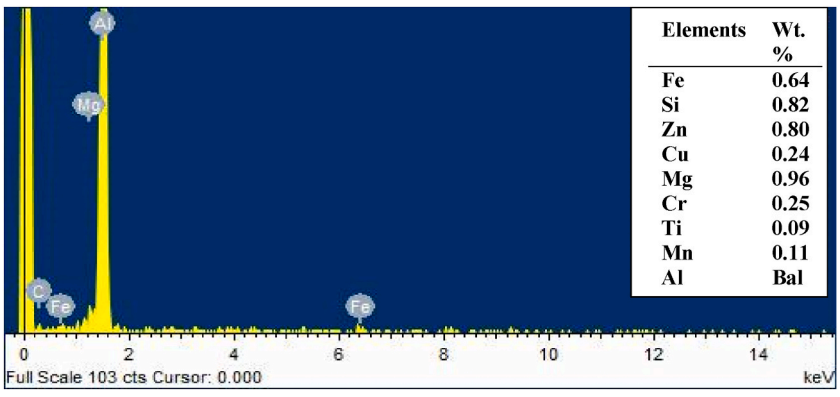

Fig. 1. EDX result depicting the elemental composition for Al 6061.

Table 3
Chemical composition of input materials.

Materials	SiO_2	MgO	Al_2O_3	Fe_2O_3	CaO	K_2O	P_2O_5	MnO_2	Other
PKA	47.32	4.18	6.91	2.95	20.15	6.75	4.08	3.54	4.16
RHA	90.21	0.67	0.28	0.59	0.32	2.1	0.08	0.00	5.75

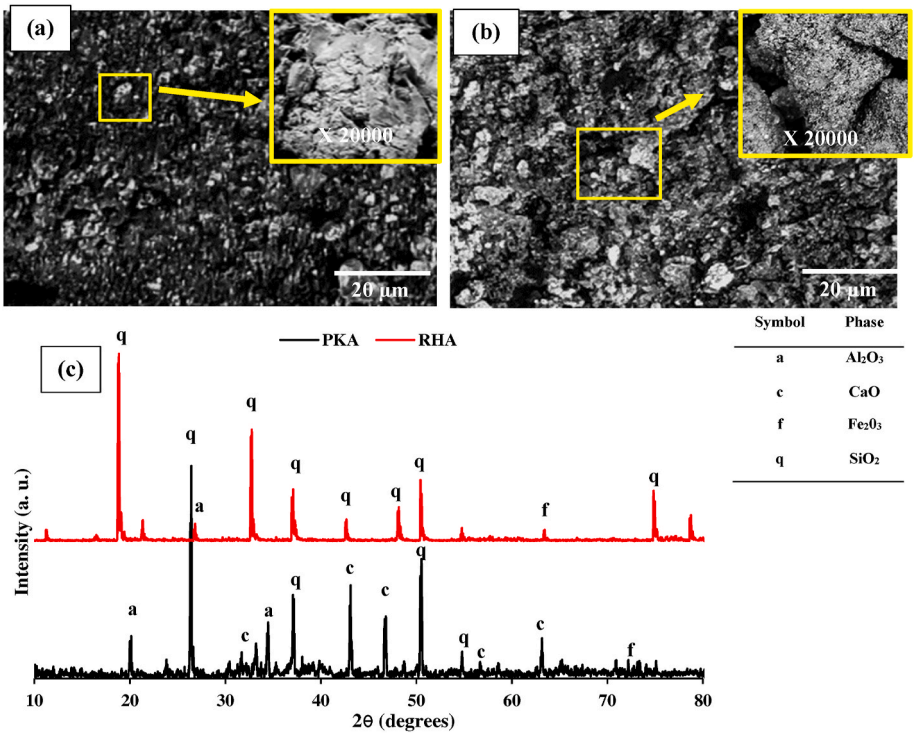

Fig. 2. Micrograph of input materials (a) PKA (b) RHA and their (c) XRD result.

morphology. The consequence of the dispersion is reflected in the property values of the samples cast at 700 °C. Authors [34–36] have shown the importance of the stir casting technique in the dispersion of particles in the molten aluminium. Also observed in the microstructure is the existence of microvoids. One result associated with the particulate reinforcement of composites is the reduction and filling of inherent pores in the matrixes. In Fig. 4a and b, the existence of pores is attributed to the minimal viscosity of the melt based during stirring. As a result, the fillers were unable to be evenly dispersed within the matrix [2]. When compared with the pure Al 6061, samples prepared with 2 wt % PKA/4 wt % RHA at 700 °C yielded 2.5, 9.1, 28.8, 45.7 and 7.8% over the control for yield strength, ultimate tensile strength, fracture toughness, impact strength, and elastic modulus. Equally, samples prepared with 4 wt % PKA/2 wt % RHA at 700 °C depicted an increment of 8.2, 16.1, 35.8, 53.5, and 11.1% over the values of pure Al 6061 in relation to the respective properties. This shows that particle distribution played an important role in enhancing property with respect to the base material. Spot EDX analysis carried out on major features of the microstructure shows the existence of waste steel debris and reinforcing particulates.

Fig. 4c and d presents the morphology of samples prepared at a stirring temperature of 800 °C composing 2 wt % PKA/6 wt % RHA and 6 wt % PKA/2 wt % RHA respectively. The microstructure shows the presence of the reinforcing agents coupled with the existence of steel flakes. As observed, the particles are dispersed within the matrix. It is revealed that microvoids are drastically reduced compared with samples cast at 700 °C. The reduced voids are responsible for the performance of the samples as compared with samples produced at 700 °C. For yield strength, ultimate tensile strength, elastic modulus, fracture toughness, and impact strength, it is estimated that the sample having 2 wt % PKA/6 wt % RHA at 800 °C exhibited 36.1, 33.3, 13.2, 106.1, and 70.8% over pure Al 6061 employed in the study. Equally, samples with doses of 6 wt % PKA/2 wt % RHA yielded 32.4, 31.2, 9.3, 110.5, and 50.9% over the pure Al 6061 as touching the respective responses initially outlined. This improvement demonstrated by the addition of reinforcement particles is imputable to the dispersion of the fillers. The trend noted in this study is corroborated by the works of the authors [37]. In another report by Ref. [10], they noted how the microstructural features of Al 6063 were improved by the introduction of palm kernel as particles. EDX spot analysis of the morphology for samples prepared at 800 °C reflected the existence of the reinforcing and steel particles void of intermetallic phase. Further observation revealed the absence of clusters and fewer presence of voids. Hence, the even distribution of the particles was claimed to aid the mechanical properties as reflected in the values indicated in Fig. 3. The EDX results

of the base alloy (matrix) reflected the existence of elements Mg, Fe, and Si, confirming the existence of the reinforcing phase (Fig. 5d).

Fig. 6 presents the morphological features and EDX spectra of samples prepared at 900 °C. As observed in the image, there is an appearance of microvoids. Authors [2], affirmed the high tendency of the existence of microvoids and blow holes at elevated temperature casting. At such temperature, there is a potency for increased gas and air entrapment, and on solidification, the gas or entrapped air is released generating voids in the matrix [38].

The EDX spectra of the base alloy is shown in Fig. 6b it shows the constituent elements like Al, Fe, Si, Mg, and Mn corroborating the EDX spectra presented in Fig. 1 for Al 6061. Different spots were identified in the image (Fig. 6a) labeled points 1, 2, and 3. Fig. 6c further revealed the identified spots under polarized light. The spot EDX result for points 1, 2, and 3 is presented in Fig. 6d–f. The elements identified are Mg and Si, for spot 1 as indicated in Fig. 5d. While Al, Fe, and Si are observed in spot 2 (Fig. 5e); Al, Fe, Mn, and Si are detected in spot 2 (Fig. 6f). The phases are identified as Mg_2Si, Al_5FeSi, and $Al_{15}Si_2(FeMn)$ corresponding to the phases earlier reported in works of literature [39–42]. These intermetallic compounds were confirmed at ICDD reference code at DB card numbers: 04-017-6811, 04-004-0004, and 01-071-4015 respectively. These phases were also corroborated by the XRD results for the sample containing 2 wt % PKA/4 wt % RHA cast at 900 °C.

The intermetallic phases occurred at casting temperature of 900 °C. Fe is observed to be present in phases 2 and 3 as confirmed in the EDX and XRD. Waste steel debris was introduced to improve the ductility of the composite. However, at elevated casting temperatures, there are interactions between the active elements resulting in the formation of intermetallic phases.

Fig. 6g–j indicate the elemental maps of the sample prepared at 900 °C (2 wt % PKA/4 wt % RHA). Fig. 6g depicts the map for Al, this confirms that Al is the base metal in the matrix as evident in the microstructure. Si is revealed to be distributed with most of the microstructure (Fig. 6h). This trend is evident since silica occupies the major phase in the reinforcement phase. Also, the Si element is identified in the intermetallic phases affirming the silica present in the phases as observed in Figures (6d – f). Fig. 6i shows the dispersion of Fe in the microstructure. The element is identified as a major element in the intermetallic phases while minor content is present in the other part of the matrix. This trend in the intermetallic phase is attributed to the reaction which occurred arising from the treatment temperature [43]. Authors [43] noted that Fe has poor solubility in aluminium, therefore, at elevated proportions, Fe has the tendency of precipitating into intermetallic phases rich in Fe content. Fig. 6j represents elemental distribution of manganese. As identified, the manganese depicted a lower proportion in the mix.

Fig. 7 highlights the morphological features and EDX spectra of samples prepared at 900 °C composing 4 wt % PKA/6 wt % RHA. The image in Fig. 7a reveals the presence of voids due to the modification of entrapped air and gases during solidification. This is typical of high-temperature casting [4]. The elemental constituent of the matrix is presented in Fig. 7b showing the existence of Mg, Si, Mn, Mg and Al similar to the EDX result of the sample 6 wt % PKA/4 wt % RHA prepared at the same temperature. Different spots labeled as 1, 2, and 3, were identified and further revealed under polarized light (Fig. 7c). From the EDX result, the composition of the

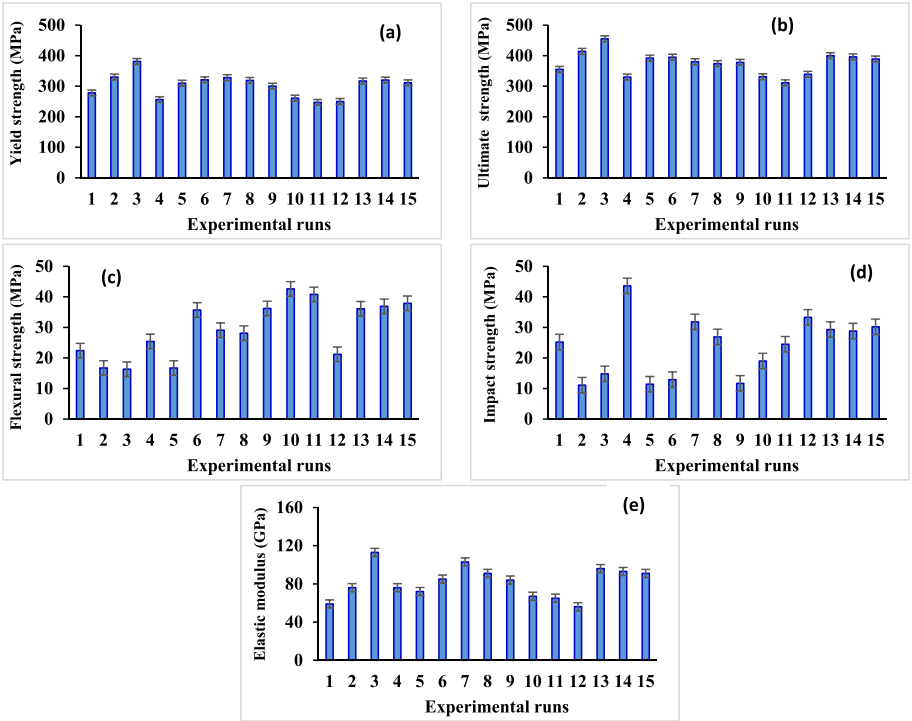

Fig. 3. Variation in (a) yield strength with respect to experimental runs (b) ultimate tensile strength with respect to experimental runs (c) flexural strength with respect to experimental runs (d) impact strength with respect to experimental runs (e) elastic modulus with respect to experimental runs.

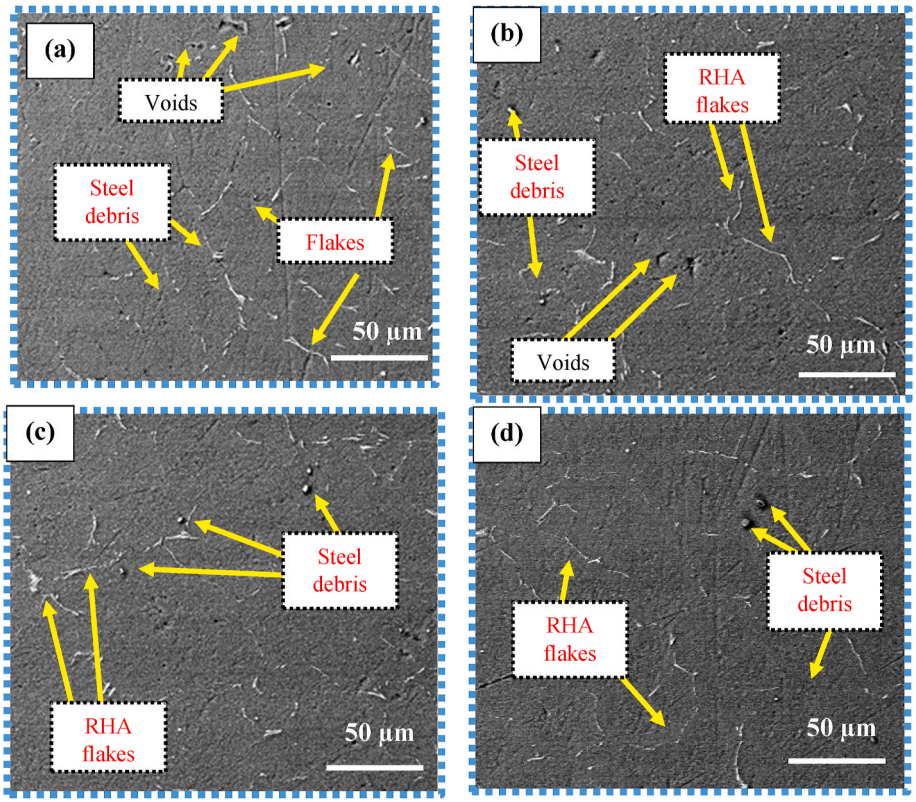

Fig. 4. Microstructural images of samples prepared at 700 °C doped with (a) 2 wt % PKA and 4 wt % RHA (b) 4 wt % PKA and 2 wt % RHA; samples prepared at 800 °C containing (c) 2 wt % PKA and 6 wt % RHA (d) 6 wt % PKA and 2 wt % RHA and (e) EDX of the matrix.

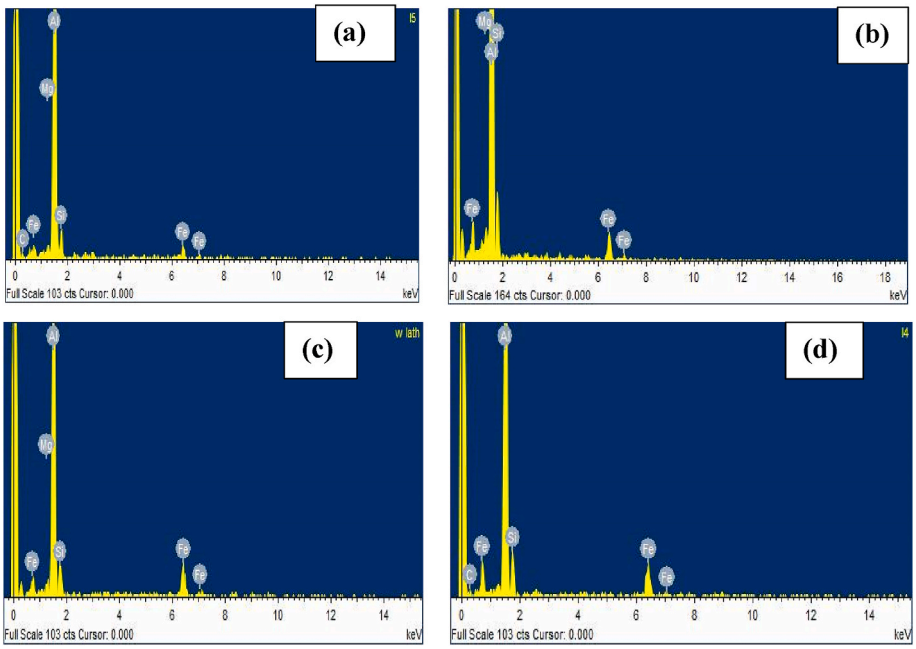

Fig. 5. Elemental composition of samples prepared at 700 °C doped with (a) 2 wt % PKA and 4 wt % RHA (b) 4 wt % PKA and 2 wt % RHA; samples prepared at 800 °C having (c) 2 wt % PKA and 6 wt % RHA (d) 6 wt % PKA and 2 wt % RHA.

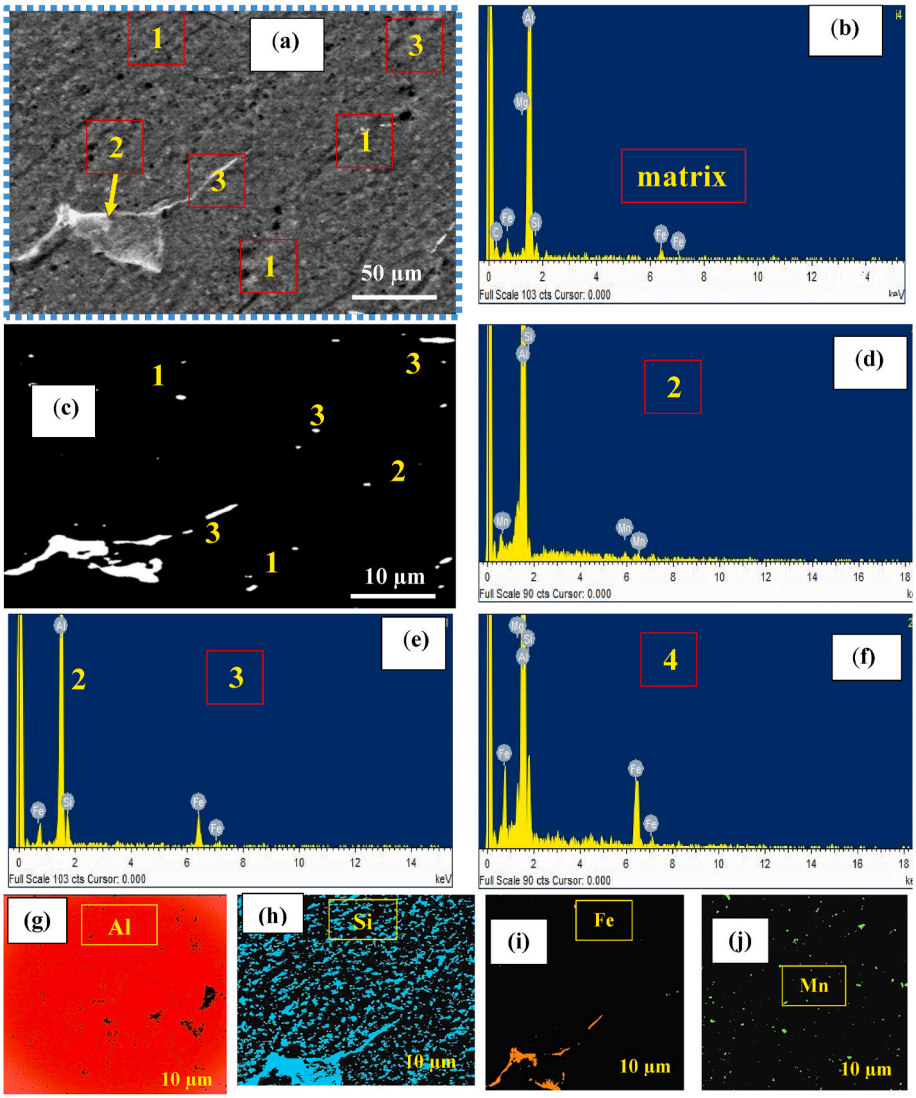

Fig. 6. Microstructure of sample cast at 900 °C with combination of 6 wt % PKA/4 wt % RHA revealed in (a) micrograph (b) EDX spectra for the base alloy (c) fluorescence morphology and EDX spectra on (d) spot 1 (e) spot 2 (f) spot 3 (g–j) elemental maps.

spots is presented in Fig. 7d–f. Similar to sample 6 wt % PKA/4 wt % RHA, the elements identified in spot 1 are Mg and Si; spot 2 Al, Fe, and Si; spot 3 Al, Fe, Mn, Si. The spots were identified as intermetallic phases of Mg_2Si, Al_5FeSi, and $Al_5S1_2(FeMn)$ respectively. Fig. 7 (g–j) presents the elemental maps in the sample. Al is identified in Fig. 7g as occupying most of the matrix based on it being the base element. Si distribution is indicated in Fig. 7h, while Fig. 7i and j portray the elemental distribution of Fe and Mn respectively.

Observing the property values in Fig. 3, sample 4 wt % PKA/6 wt % RHA performed better than 6 wt % PKA/4 wt % RHA batch by 6.5% and 5.6% with regards to yield strength and ultimate tensile strength. This is on account of higher silica content in RHA than PKA yielding better performance in sample 4 wt % PKA/6 wt % RHA. This is also held responsible for more intermetallic phases in the microstructure of sample 4 wt % PKA/6 wt % RHA than other batch prepared with 6 wt % PKA/4 wt % RHA. The features displayed in Figs. 6 and 7 in this study agrees with the microstructural features recorded in works of literature [44] in which case PKSA and RHA were infused in the aluminium matrix.

3.2. Phase identification

The peak of intensities was evident in Fig. 8a and b, showing the XRD spectra for samples cast at 700 °C show 2 wt % PKA, 4 wt % RHA, and 4 wt % PKA, 2 wt % RHA are displayed. The phases identified in the samples are SiO_2, Fe, and Al phases (with DB card numbers: 01-070-2539; 04-007-9753, and 04-013-9777 respectively). Al shows the highest peak; this confirms that the base alloy is Al alloy. Also, the SiO_2 present is derived from PKA and RHA as noted from the reinforcement materials. It is worthy of note that Fe

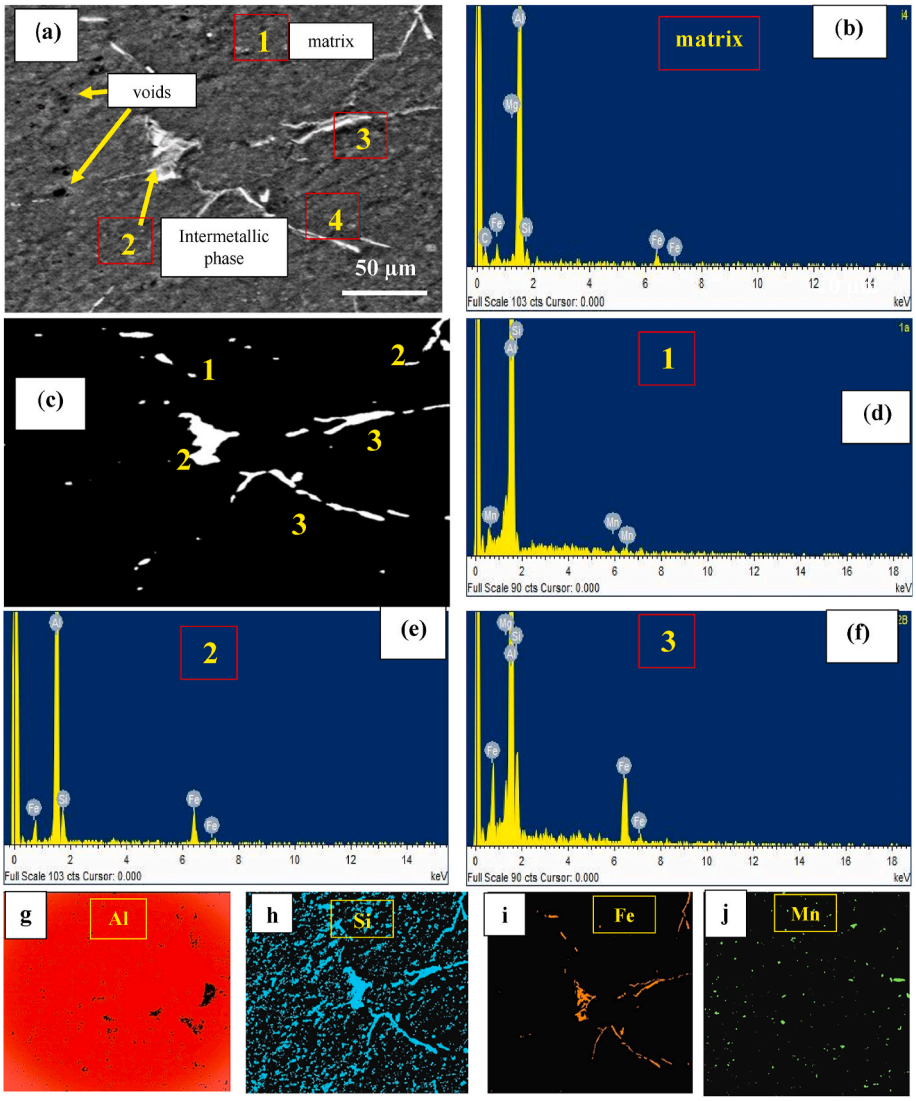

Fig. 7. Microstructure of sample cast at 900 °C with composition of 4 wt % PKA/6 wt % RHA expressed in (a) SEM image (b) EDX result for the matrix (c) fluorescence morphology and EDX results on (d) spot 1 (3) spot 2 (f) spot 3 (g–j) elemental maps.

presence is based on inherent Fe in the primary material (Al-matrix) and waste steel debris incorporated in the melt. Fig. 8b and c are XRD results for cast samples at 800 and prepared with 2 wt % PKA, 6 wt % RHA, and 6 wt % PKA, 2 wt % RHA respectively. It is observed that there is the presence of a silica phase noticeable through the peak in the spectra. Fig. 8e and f indicate the phases present in samples prepared at 900 °C with 6 wt % PKA, 4 wt % RHA, and 4 wt % PKA, 6 wt % RHA respectively.

As observed in the result, there is a presence of metallic phases of Mg_2Si, Al_5FeSi, and $Al_{15}Si_2(FeMn)$ which are intermetallic compounds. These phases earlier mentioned were established in the DB card with numbers: 04-017-6811, 04-006-3208, and 01-071-4015 respectively). It is evident that at such temperature, there exist intermetallic phases in the matrix owing to higher temperature reaction [43].

3.3. Statistical analysis

3.3.1. Analysis of variance (ANOVA)

The analysis of variance for yield strength reflecting the significance of the input parameters and their interaction is presented in Table 4.

As observed in the table, parameters A and B had significant effects on the response, in other words, PKA, RHA, and temperature reflected significant effects on yield strength. Interactions between the factors depicted insignificant effects on the response except for interaction C^2. The statistical model represented in equation (4) is stated to be consequential since the p-value is < 0.05. The

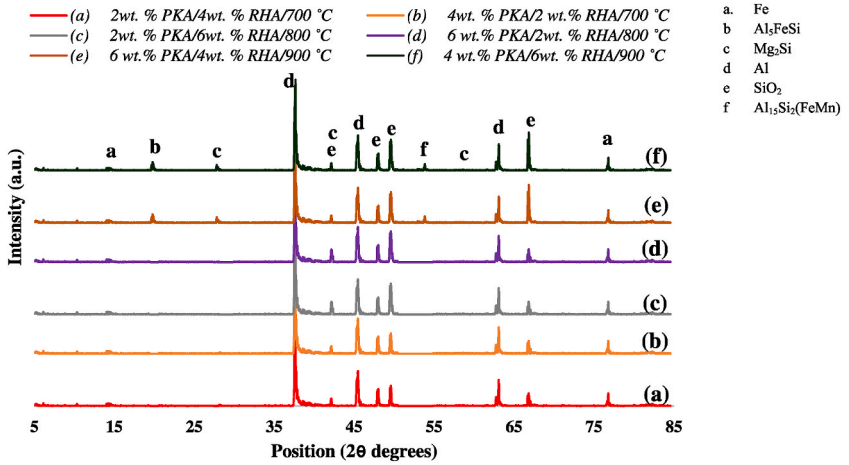

Fig. 8. Phase identification for (a) 2 wt % PKA/4 wt % RHA/700 °C (b) 4 wt % PKA/2 wt% RHA/700 °C (c) 2 wt % PKA/6 wt % RHA/800 °C (d) 6 wt% PKA/2 wt % RHA/800 °C (e) 6 wt% PKA/4 wt % RHA/900 °C and (f) 4 wt% PKA/6 wt % RHA/900 °C.

correlation coefficient which is an indication of the how the variables affect the response is 0.9862 (>0.95) signifying the model has only 1.38% variation (<5%). This shows a correlation between the variable factors and the response; hence, the model is fit for predicting yield strength response. From Table 4, the difference between R^2 (adj) and R^2 (pred) is < 0.2 depicting the model is statistically adequate to predict the response.

$$YS = -1931.2500 + 18.4375\,A + 12.2500\,B + 5.2738\,C - 0.6250\,AB - 0.0088AC + 0.0075\,BC + 0.3438A^2 + 0.2813\,B^2 - 0.0033\,C^2 \quad (4)$$

The regression model developed for the relationship between the variables and yield strength is presented in equation (4). From the results, the positive terms of the model are the ones with positive coefficients while the ones with negative signs are the negative terms. Therefore, PKA, RHA, and temperature had a significant influence on the response. The analysis of variance regarding UTS as depicted in Table 5 indicates the significant terms. Factors A, B, and C have significant contributions to the response. The same goes with interaction C^2 while other forms of interactions are insignificant.

The model (equation (5)) is termed significant since the p-value is < 0.05. The significance of the model is further confirmed by the R^2 value for the model being a value of 0.9762 (>0.95). Moreso, there is a high fitness level for the model going by the p-value of the lack of fit which is > 0.05. The difference between adjusted R^2 and predicted R^2 is > 0.2, therefore, it is indicated that the model is fit for the prediction of ultimate tensile strength.

$$UTS = -1636.2500 + 28.9375\,A + 31.8750\,B + 4.5213\,C + 1.9375\,AB - 0.0123\,AC - 0.0113\,BC - 1.7500\,A^2 - 1.5625\,B^2 - 0.0027\,C^2 \quad (5)$$

The regression model for ultimate tensile strength is presented in equation (5). Factors A, B, and C have a positive coefficient, it, therefore, means that increasing values of PKA, RHA, and temperature are favorable to ultimate tensile strength.

The Table showing the variation in the analysis variance on fracture toughness is indicated in Table 6. The model of fracture

Table 4
Analysis of variance on the yield strength of developed samples.

Source	Sum of Squares	df	Mean Square	F-value	p-value	
Model	18727.11	9	2080.79	24.79	0.0037	significant
A-A	4371.12	1	4371.12	52.08	0.0020	
B–B	10368.00	1	10368.00	123.52	0.0004	
C–C	1900.13	1	1900.13	2.27	0.0268	
AB	25.00	1	25.00	0.30	0.6142	
AC	12.25	1	12.25	0.15	0.7219	
BC	9.00	1	9.00	0.11	0.7597	
A^2	6.05	1	6.05	0.07	0.8016	
B^2	4.05	1	4.05	0.05	0.8369	
C^2	3406.05	1	3406.05	40.58	0.0031	
Residual	335.75	4	83.94			
Lack of Fit	331.25	3	110.42	24.54	0.1471	not significant
Pure Error	4.50	1	4.50			
Cor Total	19062.86	13				
$R^2 = 0.9824$		R^2 (adj) = 0.9424		R^2 (pred) = 0.9210		

Table 5
Analysis of variance on ultimate tensile strength.

Source	Sum of Squares	df	Mean Square	F-value	p-value	
Model	19194.75	9	2132.75	31.68	0.0023	significant
A-A	5151.12	1	5151.12	76.53	0.0009	
B–B	10512.50	1	10512.50	156.17	0.0002	
C–C	903.13	1	903.13	13.42	0.0215	
AB	240.25	1	240.25	3.57	0.1319	
AC	25.00	1	25.00	0.37	0.5752	
BC	20.25	1	20.25	0.30	0.6125	
A^2	156.80	1	156.80	2.33	0.2016	
B^2	125.00	1	125.00	1.86	0.2446	
C^2	2332.80	1	2332.80	34.66	0.0042	
Residual	269.25	4	67.31			
Lack of Fit	261.25	3	87.08	10.89	0.2184	not significant
Pure Error	8.00	1	8.00			
Cor Total	19464.00	13				
$R^2 = 0.9762$		R^2 (adj) = 0.9550		R^2 (pred) = 0.8736		

toughness is indicated to be significant going by the p-value estimated to be as < 0.05 (Table 6).

$$FT = -70.5750 + 12.6250\,A + 14.8813\,B - 0.1124\,C - 0.1563\,AB + 0.0009\,AC + 0.0008\,BC - 1.7688\,A^2 - 1.9875\,B^2 + 0.0000\,C^2 \quad (6)$$

The regression model for fracture toughness is depicted in equation (6). In the model, factors A and B, have positive coefficient while factor C possess negative coefficient. It, therefore, implies that PKA and RHA are favorable to fracture toughness while the temperature is detrimental to the response.

The ANOVA for impact strength is illustrated in Table 7. As presented, factors A, and B, that is PKA and RHA contributed significantly to the magnitude of impact strength. However, temperature showed an insignificant influence on the response. Al interaction terms are insignificant except for interaction C^2.

The model presented in equation (7) is termed significant since the p-value is < 0.05. The significance of the model is further confirmed by the R^2 value for the model being a value of 0.9749 (>0.95). Equally, there is a high level of fitness for the model going by the p-value of the lack of fit which is > 0.05. The deviation between adjusted R^2 and predicted R^2 is > 0.2. In that case, it is deduced that the model is fit for the prediction of ultimate tensile strength.

$$UTS = -679.1250 + 6.5500\,A + 3.2188\,B + 1.7856\,C - 0.0188\,AB - 0.0081\,AC - 0.0133\,BC - 0.4250\,A^2 + 0.4813\,B^2 - 0.0011\,C^2 \quad (7)$$

The regression model for impact strength as a measure of impact energy absorbed is presented in equation (7). Factors A, B, and C have a positive coefficient, it, therefore, means that increasing values of PKA, RHA, and temperature are favorable to ultimate tensile strength. The analysis of variance regarding flexural strength as indicated in Table 8 depicts the significant terms. Factors A, B, and C have significant contributions to the response. A similar trend goes with interaction C^2 while other forms of interactions are

Table 6
Analysis of variance on fracture toughness.

Source	Sum of Squares	df	Mean Square	F-value	p-value	
Model	1195.18	9	132.80	385.62	<0.0001	significant
A-A	67.28	1	67.28	195.37	0.0002	
B–B	34.86	1	34.86	101.23	0.0005	
C–C	766.36	1	766.36	2225.37	<0.0001	
AB	1.56	1	1.56	4.54	0.1002	
AC	0.12	1	0.12	0.36	0.5830	
BC	0.09	1	0.09	0.26	0.6361	
A^2	160.18	1	160.18	465.13	<0.0001	
B^2	202.25	1	202.25	587.29	<0.0001	
C^2	0.0080	1	0.0080	0.02	0.8862	
Residual	1.38	4	0.3444			
Lack of Fit	1.06	3	0.3525	1.10	0.5890	not significant
Pure Error	0.3200	1	0.3200			
Cor Total	1196.55	13				
$R^2 = 0.9888$		R^2 (adj) = 0.9763		R^2 (pred) = 0.9648		

The p-value of the lack of fit is > 0.05 indicating the lack of fit is marginal, significant. It, reveals that the model has a good degree of fitness. The R^2 value for fracture toughness being 0.9888 (>0.95) depicts the model can represent 98.88% of the variation in the response. It further shows that experimental error is small. Factors A, B, and C reflected significant contributions to fracture toughness (p-value <0.05). Interaction terms are insignificant except for interactions A^2 and B^2. The difference between the value of adjusted R^2 and predicted R^2 is > 0.2 and by implication, the model can be exploited for prediction of fracture toughness between the ranges of values for the variable inputs.

Table 7
Analysis of variance on impact strength.

Source	Sum of Squares	df	Mean Square	F-value	p-value	
Model	1259.88	9	139.99	17.30	0.0073	significant
A-A	375.38	1	375.38	46.38	0.0024	
B–B	416.16	1	416.16	51.42	0.0020	
C–C	20.80	1	20.80	2.57	0.1842	
AB	0.02	1	0.02	0.0028	0.9605	
AC	10.56	1	10.56	1.31	0.3170	
BC	28.09	1	28.09	3.47	0.1359	
A^2	9.25	1	9.25	1.14	0.3453	
B^2	11.86	1	11.86	1.47	0.2927	
C^2	354.48	1	354.48	43.80	0.0027	
Residual	32.37	4	8.09			
Lack of Fit	32.25	3	10.75	85.99	0.0791	not significant
Pure Error	0.1250	1	0.13			
Cor Total	1292.25	13				
$R^2 = 0.9749$		R^2 (adj) = 0.9186		R^2 (pred) = 0.8003		

insignificant.

The model (equation (8)) is termed significant since the p-value is < 0.05. The significance of the model is further confirmed by the R^2 value for the model being a value of 0.9851 (>0.95). More so, there is a high level of fitness for the model going by the p-value of the lack of fit which is > 0.05. The deviation between adjusted R^2 and predicted R^2 is > 0.2, therefore, it is indicated that the model is fit for the prediction of flexural strength.

$$EM = -1495.500 + 7.4375\,A + 5.5625\,B + 3.9125\,C - 0.3125\,AB - 0.0050\,AC + 0.0000\,BC + 0.1563\,A^2 + 0.1563\,B^2 - 0.0025\,C^2 \quad (8)$$

The regression model for flexural strength is illustrated in equation (8). Factors A, B, and C have a positive coefficient, it, therefore, means that increasing values of PKA, RHA, and temperature are favorable to ultimate tensile strength. It is evident in the trend of results obtained that the input variables palm kernel ash and rice husk ash played a role in the responses. The contributing influence of the temperature in determining the trend of the response is also important [45].

3.3.2. Diagnostic plot

The diagnostic plot displayed in Fig. 9 is the normal distribution plot for Fig. 9a yield strength, Fig. 9b ultimate tensile strength, Fig. 9c fracture toughness, Fig. 9d impact strength, and Fig. 9e elastic modulus respectively. In the figures, the residual plots are distributed along the meal line (red line). This indicates the fitness of the model to represent the data for each of the responses. Fig. 10 presents the residual vs predicted plot and it is noted that the plots are located randomly around the zero line for all responses. There is, therefore, no correlation between the data further depicting good models [24].

3.4. Surface and contour plots

3.4.1. Yield strength

Fig. 11 exhibits the surface plot (11a) as well as the contour plot (11b) with regard to yield strength. The interaction existing between PKA and RHA and their influence on the yield strength of the composite at a fixed stirring temperature of 800 °C is revealed in

Table 8
Analysis of variance on impact strength.

Source	Sum of Squares	df	Mean Square	F-value	p-value	
Model	3675.46	9	408.38	89.51	0.0003	significant
A-A	378.12	1	378.12	82.88	0.0008	
B–B	990.13	1	990.13	217.01	0.0001	
C–C	180.50	1	180.50	39.56	0.0033	
AB	6.25	1	6.25	1.37	0.3068	
AC	4.00	1	4.00	0.88	0.4021	
BC	0.0000	1	0.0000	0.00	1.0000	
A^2	1.25	1	1.25	0.27	0.6283	
B^2	1.25	1	1.25	0.27	0.6283	
C^2	1940.45	1	1940.45	425.30	0.0000	
Residual	18.25	4	4.56			
Lack of Fit	13.75	3	4.58	1.02	0.6052	not significant
Pure Error	4.50	1	4.50			
Cor Total	3693.71	13				
$R^2 = 0.9851$		R^2 (adj) = 0.9739		R^2 (pred) = 0.9456		

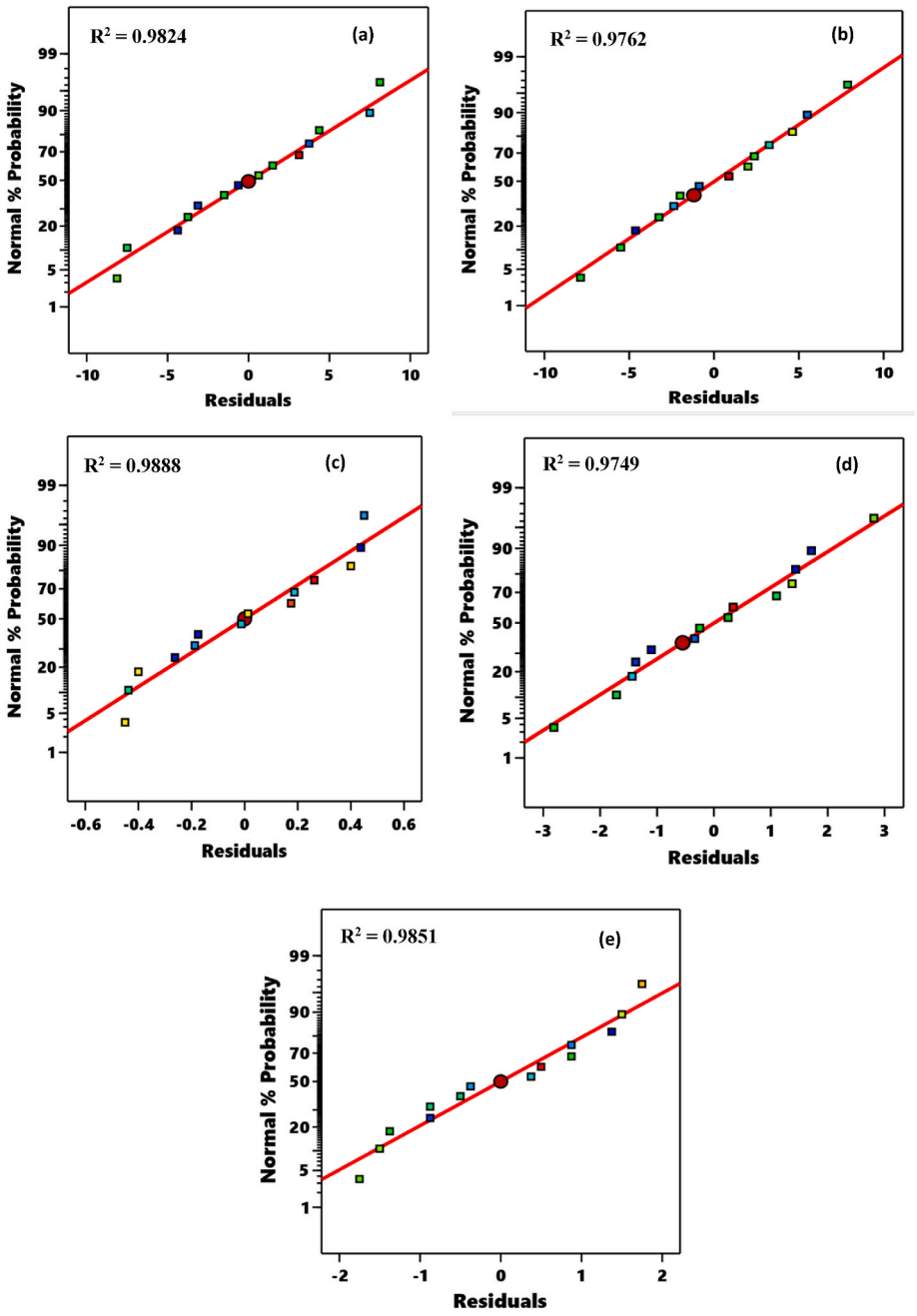

Fig. 9. Normal distribution plot for responses (a) yield strength (b) ultimate tensile strength (c) fracture toughness (d) impact strength (e) elastic modulus.

Fig. 11a.

The interaction between 2 and 6 wt % PKA and 2–6 wt % RHA caused progressive strength enhancement exhibiting a linear interaction profile. Portion "A" in Fig. 11b is categorized as the optimum region where yield strength can be optimized. Therefore, yield strength >360 is realizable within the range of 4.2–6 wt % PKA at 4.9 and 6 wt % RHA. Hence, optimum yield strength for the inter-activity between PKA and RHA at 800 °C stirring temperature can be achieved in the range of 4.2–6 wt % for PKA and 4.9 and 6 wt % for RHA.

On the other hand, the interplay between PKA and stirring temperature at a constant RHA dose of 4 wt % is illustrated in Fig. 11c while Fig. 11c displays the contour plot for the interaction. The introduction of 2–6 wt% PKA in the melt at a temperature range of 700–800 °C is favorable for yield strength and ensuing strength improvement. Nonetheless, the input of the same proportion of PKA between 800 and 900 °C results in the minimization of strength. It, therefore, depicts that PKA exhibited linear interaction trending

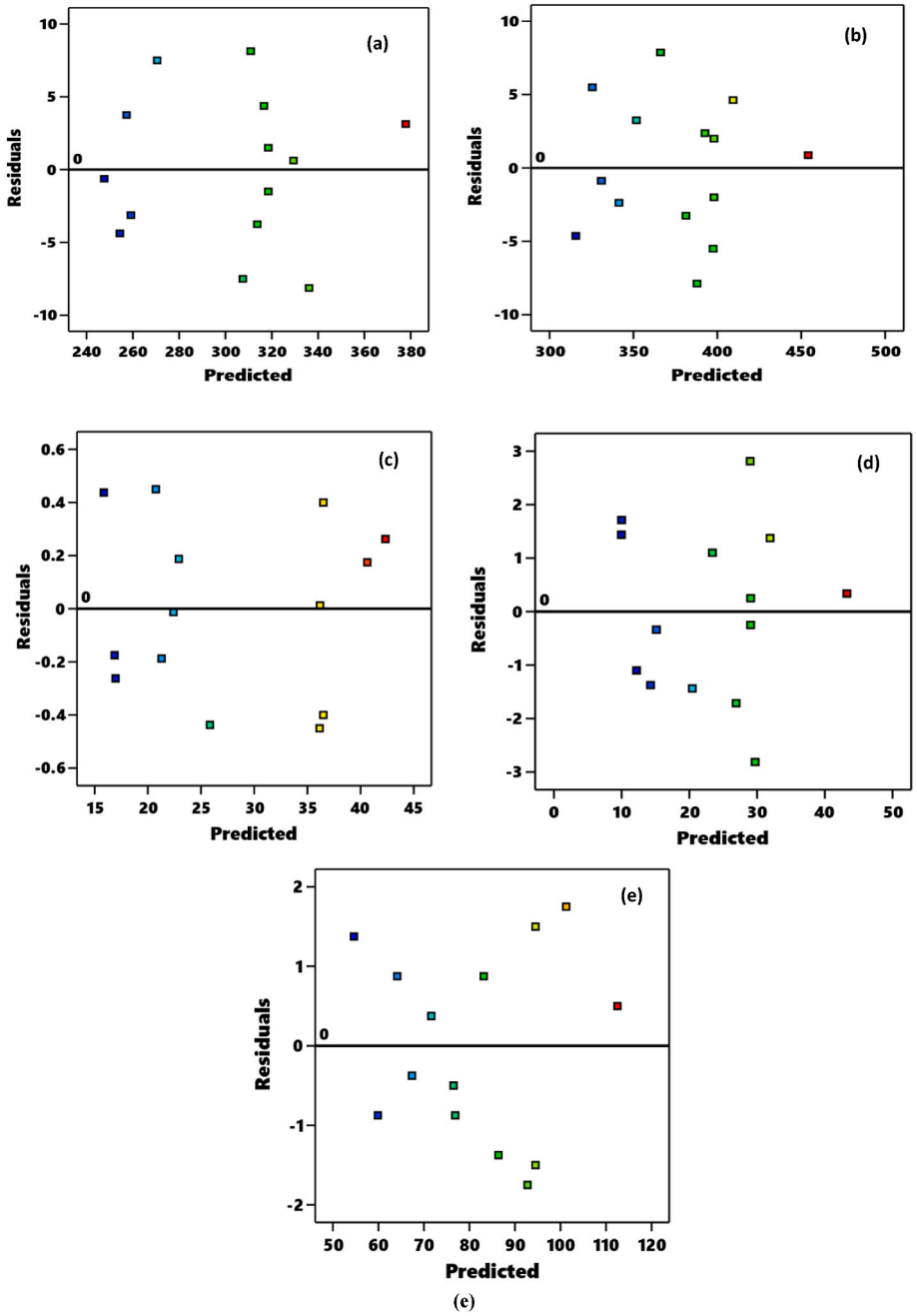

Fig. 10. Residuals against predicted plot for responses (a) yield strength (b) ultimate tensile strength (c) fracture toughness (d) impact strength (e) elastic modulus.

upward while temperature manifested a parabolic profile. From Fig. 11d, the zone tagged B is the optimum zone for yield strength with regard to the interaction. In maximizing yield strength, PKA should be in the range of 5.6–6 wt % at the temperature range of 755–825 °C.

Fig. 11e and f displays the surface plot and the contour plot for the interaction between RHA and temperature when keeping PKA at 4 wt %. Infusion of 2–6 wt % RHA in the melt at a constant PKA of 4 wt % and within a temperature range of 700–800 resulted in strength improvement, whereas, the same quantity within 800 and 900 resulted in strength depreciation. In that case, while RHA portrayed a linear profile of positive gradient, temperature ensued an inverted parabolic profile. The portion tagged "C" in Fig. 11f is a portion in which the strength performance can be maximized (>340 MPa) in the range of 5.3–6 wt % RHA and 745–870 °C.

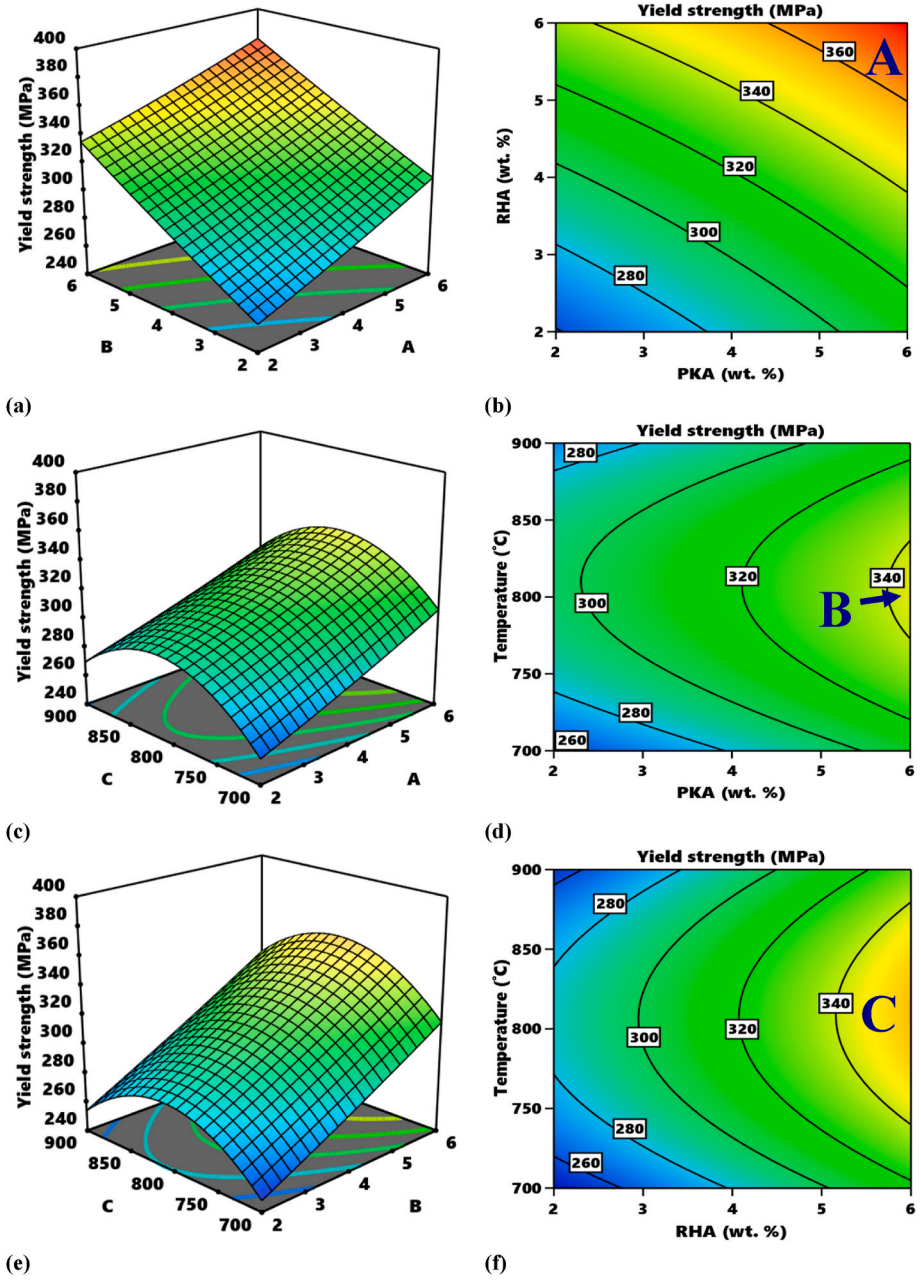

Fig. 11. Variations in yield strength with respect to the input variables for (a) surface plot showing interaction between B and A (b) surface plot showing interaction between RHA and PKA (c) Contour plot showing interaction between C and A (d) surface plot showing interaction between temperature and PKA (e) surface plot showing interaction between C and B (f) contour plot showing interaction between temperature and RHA.

3.4.2. Ultimate tensile strength

Fig. 12a demonstrates the surface plot for the interaction between PKA and RHA in relation to the influence of the interaction between PKA and RHA on yield strength. As revealed, 2–4 wt% PKA interacting with 2–4 wt % RHA led to strength improvement. The two inputs exhibited a linear profile.

In Fig. 12b, optimum zone "A" is the zone for achieving strength >440 MPa for the response achievable in the range of 4.7–6% for PKA and 5.2–6% for RHA. In that case, strength between 440 and 460 MPa is attainable when combining PKA and RHA in the range of 4.7–6% for PKA and 2–6% for RHA. Fig. 12c shows the surface plot displaying the trend of PKA against temperature when keeping RHA constant at 4 wt %. 2–6 wt% PKA added into the melt ranging 700–800 °C at constant 4 wt % RHA ensued improving strength even as same proportion of PKA at 800–900 °C resulted in strength reduction. In Fig. 12d, the portion marked "B" is tagged as the optimum zone for attaining a strength range of 400–420 MPa. This is realizable between 4.2 and 6% for PKA and 740–885 °C for temperature.

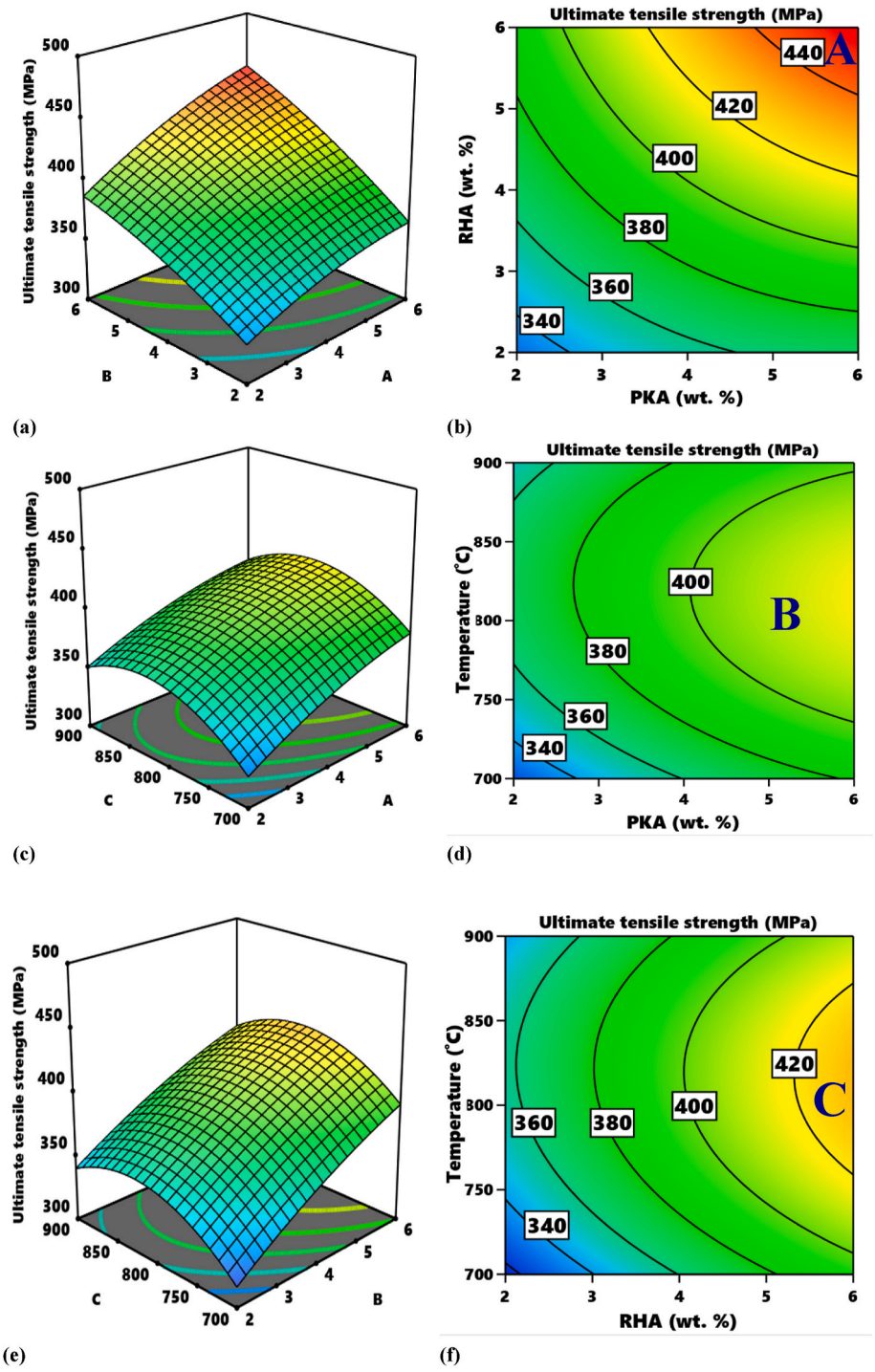

Fig. 12. Variations in ultimate tensile strength with respect to the input variables for (a) contour plot showing interaction between B and A (b) surface plot showing interaction between RHA and PKA (c) Contour plot showing interaction between C and A (d) surface plot showing interaction between temperature and PKA (e) surface plot showing interaction between C and B (f) contour plot showing interaction between temperature and RHA.

Hence the blend of 4.2–6% PKA with 4% RHA at a temperature range of 740–885 °C yields the optimum strength range. Fig. 12e demonstrates the surface plot for interaction RHA vs stirring temperature when keeping PKA constant at 4 wt %. It is observed that 2–6 wt% RHA added to 4 wt % PKA at a temperature range of 700–800 °C favors strength improvement while the same range of particles at a temperature variable of 800–900 °C led to depreciation in strength. The region marked "C" in Fig. 12f presents the portion in which

maximum strength is attainable between 420 and 440 MPa. The implication is that strength can be optimized in the range of 5.5–6% for RHA, 4 wt % PKA, and a temperature range of 760–870 °C.

3.4.3. *Fracture toughness*

Fig. 13 exhibits the surface plot (13a) as well as the contour plot (13b) with respect to the fracture toughness of the composite. The

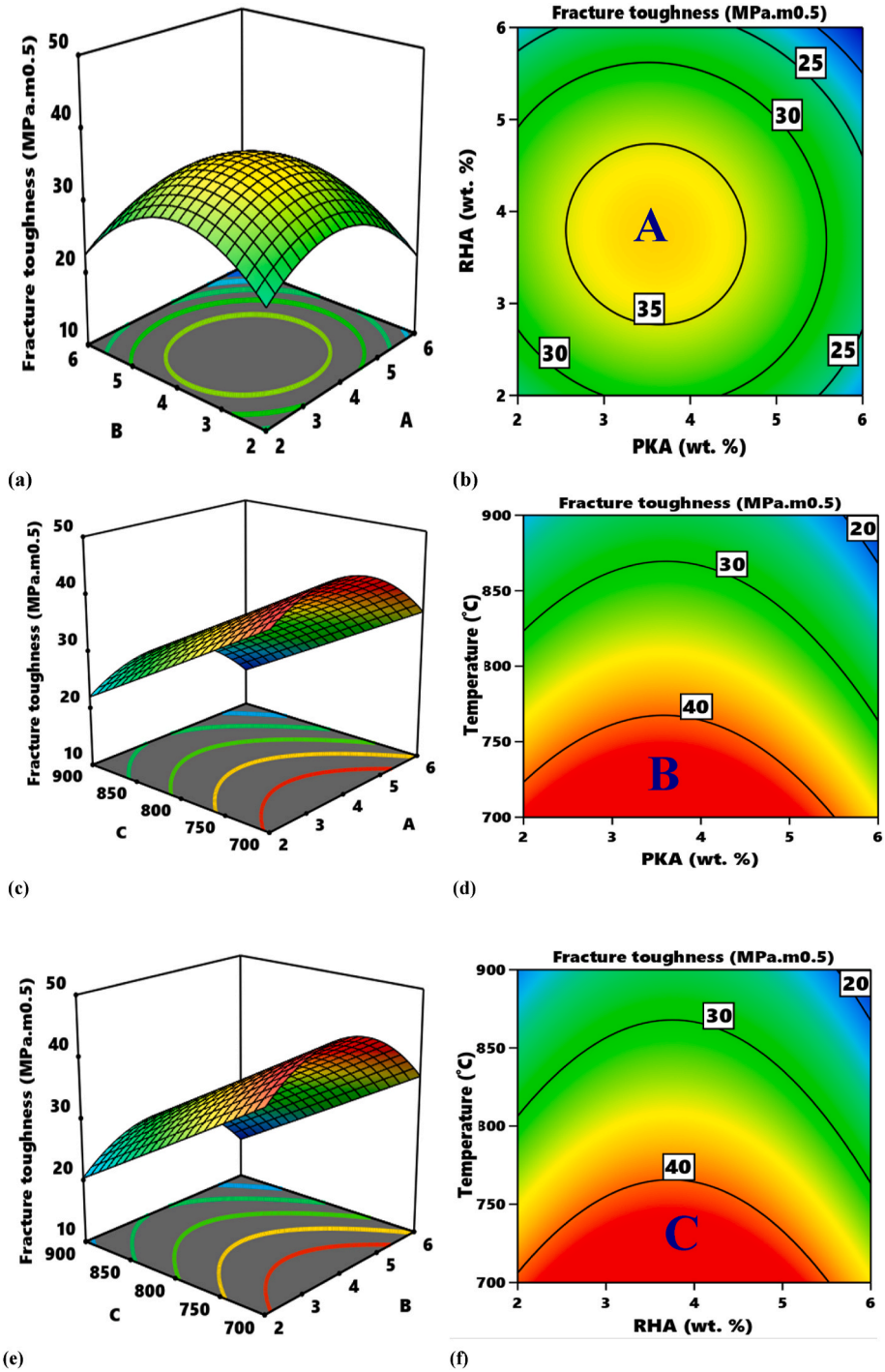

Fig. 13. Variations in fracture toughness with respect to the input variables (a) surface plot showing interaction between B and A (b) surface plot showing interaction between RHA and PKA (c) Contour plot showing interaction between C and A (d) surface plot showing interaction between temperature and PKA (e) surface plot showing interaction between C and B (f) contour plot showing interaction between temperature and RHA.

interaction existing between PKA and RHA and the effect on the fracture toughness of the composite at a fixed stirring temperature of 800 °C is shown in Fig. 13a.

The interplay between 2 and 4 wt % PKA and 2–4 wt % RHA ensued progressive strength enhancement. A blend of 4–6 wt% PKA

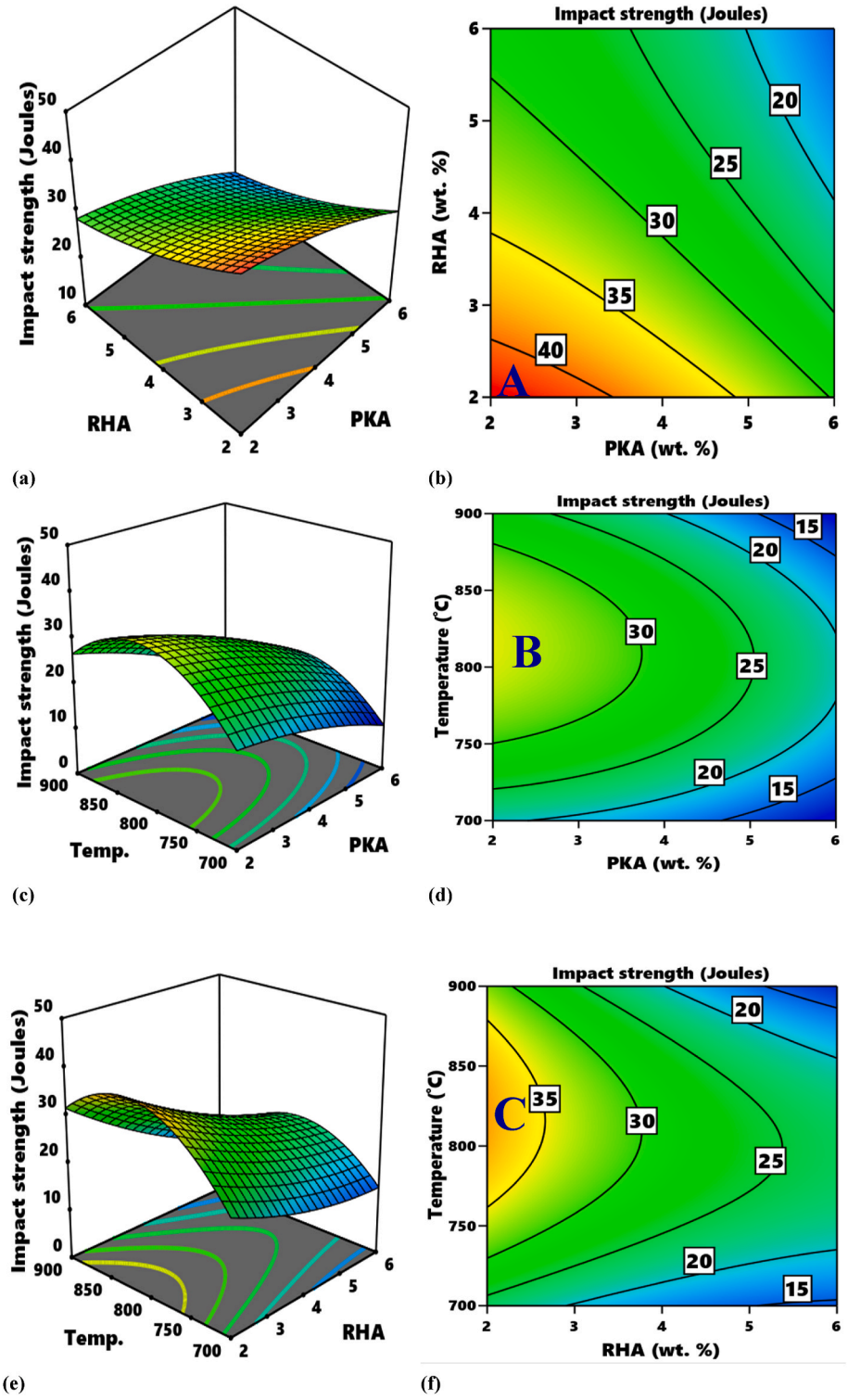

Fig. 14. Response surface and contour plots reveal the effects of interactions on impact strength as represented by interactions (a, b) PKA vs RHA (c, d) PKA vs stirring temperature (e, f) RHA vs stirring temperature.

and 4 – 6 wt % RHA at 800 °C induces strength reduction. The two inputs displayed an inverted parabolic profile, while Portion "A" in Fig. 13b is categorized as the optimum region where fracture toughness can be optimized. Therefore, fracture toughness value between 35 and 40 MPa $m^{0.5}$ is realizable within the range of 2.4–4.6 wt % PKA, 2.8 and 4.5 wt % RHA. Hence, optimum yield strength for the interaction between PKA and RHA at 800 °C stirring temperature can be achieved in the range of 2.4–4.6 wt % for PKA at 42.8 and 4.5 wt % for RHA. The interplay between PKA and stirring temperature at a constant RHA dose of 4 wt % is illustrated in Fig. 13c while Fig. 13c displays the contour plot for the interaction. The introduction of 2 – 4 wt % PKA is favorable to the enhancement of the fracture toughness while 4 – 6 wt% is detrimental to the response. A progressive increase in strength led to a reduction in fracture toughness. PKA displayed an inverted parabolic profile even as temperature displayed a negative linear profile. From Fig. 13d, the zone tagged B is

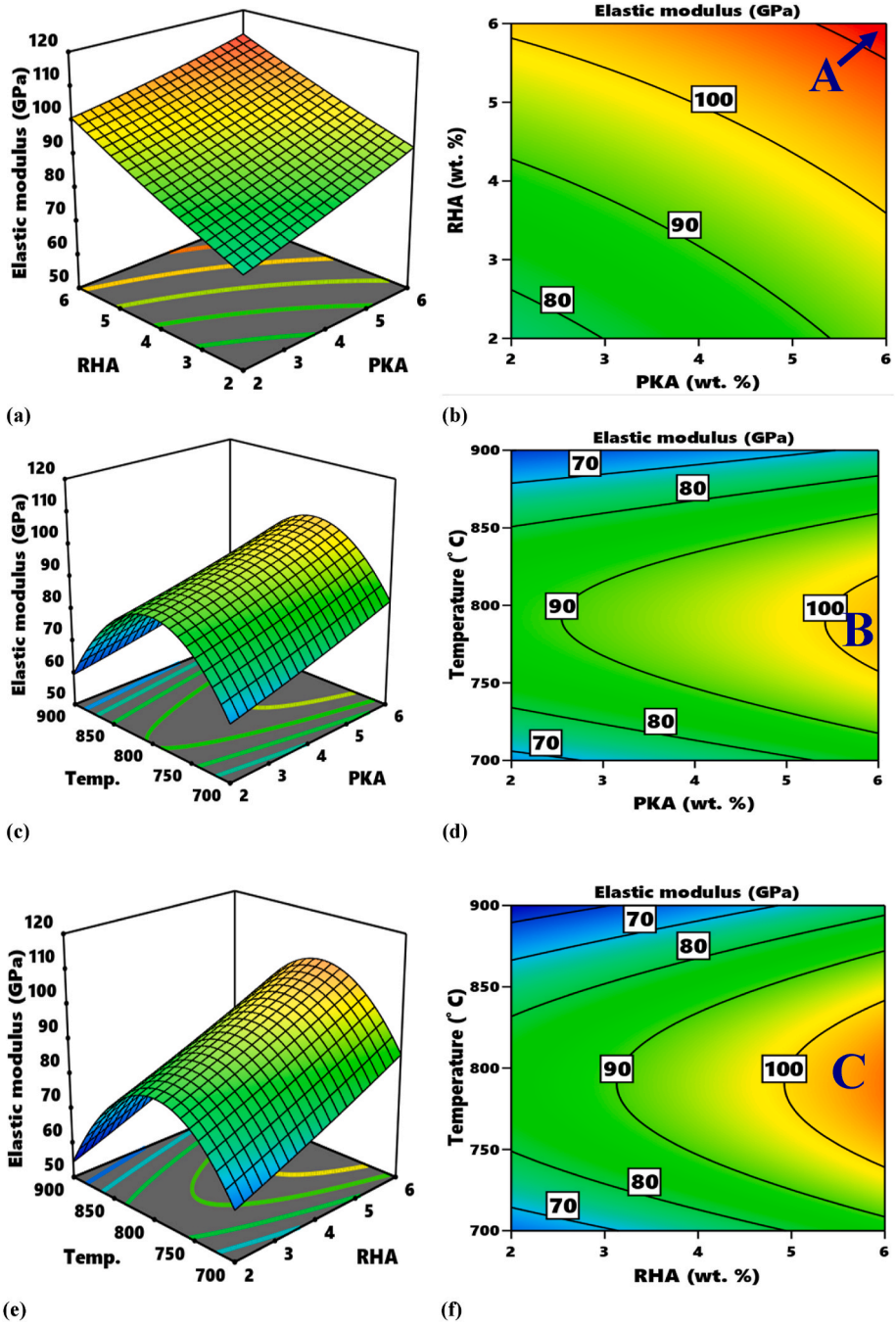

Fig. 15. Response surface and contour plots revealing effects of interactions on elastic modulus as represented by interactions (a, b) PKA vs RHA (c, d) PKA vs stirring temperature (e, f) RHA vs stirring temperature.

the optimum zone for fracture toughness response with regard to the interaction. Maximizing response is attainable in the range of 2–5.4 wt % at a temperature range of 700–765 °C.

Fig. 13e and f displays the surface plot and the contour plot for the interaction between RHA and temperature when keeping PKA at 4 wt %. Infusion of 2–4 wt % RHA in the melt at constant PKA of 4 wt % and within a temperature range of 700–900 °C resulted in strength enhancement, whereas, 4–6 wt % RHA within the same temperature range ensues strength deprecation. In that case, while RHA portrayed an inverted parabolic profile, temperature showed a negative linear profile. The part tagged "C" in Fig. 13f indicates the portion where the response can be maximized between 40 and 50 MPa $m^{0.5}$ in the range of 2–5.5 wt % RHA and 700–760 °C.

3.4.4. Impact strength

Fig. 14a shows the surface plot for the interaction between PKA and RHA in relation to the influence of the interaction between PKA and RHA on impact strength. As revealed, 2–6 wt% PKA improves impact strength slightly while 2–6 wt % RHA led to a slight decrease in strength.

The input variables exhibited an inverse interaction profile. In Fig. 14b, optimum zone "A" is the zone for achieving strength >40 J for the response achievable in the range of 2–3.3 wt % for PKA and 2–2.6 wt % for RHA. In that case, strength between 40 and 45 J is attainable when combining PKA and RHA in the range of 2–3.3 wt % for PKA and 2–2.6 wt % for RHA. Fig. 14c featured the surface plot showing the influence of PKA vs temperature affecting the response when keeping RHA constant at 4 wt %. Temperature range of 700–800 °C contribute to a boost in strength while 800–900 °C spawned a strength decrease. 2–6 wt % PKA infused into the melt between 700 and 800 °C at constant 4 wt % RHA strength decrease. In Fig. 14d, portion marked B is tagged as the optimum zone for attaining a strength range of 30–35 J. This is realizable between 2 and 3.6 wt % for PKA and 751–880 °C for temperature. Hence the blend of 2–3.6 wt % PKA with 4% RHA at a temperature range of 751–880 °C yields the optimum strength range.

Fig. 14e display the plot for interaction RHA against stirring temperature when keeping PKA constant at 4 wt %. It is observed temperature range of 700–800 °C favors strength enhancement while a temperature ranges between 800 and 900 °C is detrimental to the strength. The region marked "C" in Fig. 14f presents the portion in which maximum strength is attainable between 35 and 40 J. This implies that strength can be optimized in the range of 2–2.5 wt% for RHA, 4 wt% PKA, and a temperature range of 760–870 °C.

3.4.5. Elastic modulus

Fig. 15a demonstrates the surface plot for the interaction between PKA and RHA in relation to the influence of the interaction between PKA and RHA on elastic modulus. As revealed, 2–6 wt% PKA interacting with 2–6 wt % RHA led to strength improvement.

The two inputs exhibited a positive gradient linear profile. In Fig. 15b, optimum zone "A" is the zone for achieving strength >110 GPa for the response achievable in the range of 5.6–6 wt % for PKA and 5.7–6 wt % for RHA. In that case, a modulus value between 110 and 120 MPa is attainable when combining PKA and RHA in the range of 5.6–6 wt % for PKA and 5.7–6 wt % for RHA. Fig. 15c features the surface plot and the influence of PKA vs temperature affecting the response when keeping RHA constant at 4 wt %. 2–6 wt% PKA infused into the melt between 700 and 800 °C at constant 4 wt % RHA ensued improvement in the modulus responses even as same proportion of PKA at 800–900 °C resulted in strength reduction. In Fig. 15d, the portion marked "B" is tagged as the optimum zone for attaining a modulus range of 100–110 GPa. This is realizable between 4.8 and 6 wt% for PKA and 745–830 °C for temperature. Hence the blend of 4.8–6 wt % PKA with 4% RHA at a temperature range of 745–830 °C yields the optimum response range. Fig. 15e demonstrates the surface plot for interaction RHA vs stirring temperature when keeping PKA constant at 4 wt %. It is observed that 2–6 wt% RHA infused with 4 wt % PKA at a temperature range of 700–800 °C favors a boost in elastic modulus while the same range of particles at a temperature range of 800–900 °C showed a depreciation in the response. The region marked "C" in Fig. 15f presents the portion in which maximum modulus is attainable between 100 and 110 GPa. It can be inferred that the modulus can be optimized in the range of 4.9–6 wt % for RHA, 4 wt % PKA, and a temperature range of 740–820 °C.

3.5. Optimization and results validation

As previously reported [24], optimization was done to determine the optimum combination of the input variables in realizing the balance performance of the composite [44]. The constraints for the optimization procedure are indicated in Table 9. The result obtained from the optimization process is presented in Fig. 16. The optimum condition is attained as 4.03095 wt % PKA, 5.1207 wt % RHA blended with 1 wt % steel debris at 786.957 °C temperature. Predicted responses are 338.069 MPa, 415.133 MPa, 34.0482 MPa $m^{0.5}$, 25.3134 J, and 101.228 GPa for yield strength, ultimate tensile strength, fracture toughness, impact strength, and elastic modulus in that order.

An experiment to validate the model's predictions was carried effected with the predicted optimum conditions. Three samples were fabricated for each test and the mean result obtained was recorded. The result of the validation experiment include 326.51 MPa for yield strength, 402.64 MPa for ultimate tensile strength, 35.11 MPa $m^{0.5}$ for fracture toughness, 24.71 J for impact strength and 98.4 GPa. The error calculated for each response is less than 5%, thereby validating the models to be statistically fit in response prediction.

3.6. Microstructural features of samples prepared at optimum condition

The microstructural image (Fig. 17a) of the sample prepared at 4.03 wt% PKA/5.12 wt % RHA alongside 4 wt% waste steel debris at 786.96 °C casting temperature.

As indicated in the image, the reinforcing particles are distributed within the matrix effect which reflected an improvement in property as compared with the pure Al-6061 matrix. The EDX spectra presented in Fig. 17b depicts Al as the major constituent being

Table 9
Optimization criteria.

Name	Goal	Lower Limit	Upper Limit	Importance
PKA	is in range	2	6	3
RHA	is in range	2	6	3
Temp.	is in range	700	900	3
YS	maximize	247	381	3
UTS	maximize	311	455	3
FT	maximize	16.3	42.6	3
IS	maximize	11.1	43.6	3
EM	maximize	56	113	3

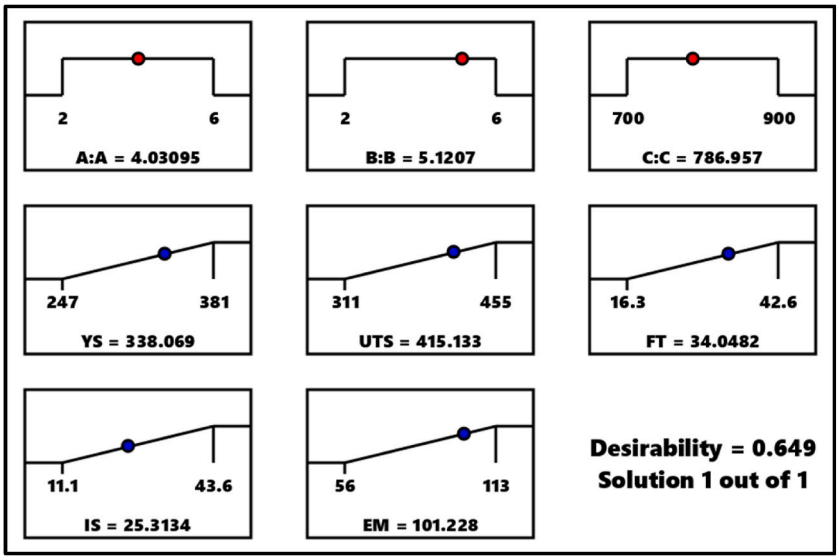

Fig. 16. Optimization ramp.

the matrix. Notably, the presence of elements such as Si and Fe, which are the major elemental constituents of the reinforcing particles is evident in the EDX spectrum. The XRD spectra are shown in Fig. 17c–f revealed the elemental distribution of Mn, Si, Fe and Al respectively (as contained in the DB card number: 01-078-5052, 01-081-8772, 01-077-2110, and 01-081-6623). The high intensity in the diffraction pattern is evident in the peak of Al representing a preferred orientation of micro crystallites. It is observed that this peak reduces from the monolithic alloy (matrix) to the hybridized composites. This shows that PKA and RHA (reinforcements) contribute towards this shift. This trend was also reported in the findings of authors [46] from their studies. A notable peak of Si was also observed, indicating the presence of silicon-based elements in the reinforcement and the matrix itself. Fe and Mn are sparingly distributed, this is evident from the base alloy composition (as contained in the DB card number: 00-005-0565 and 01-081-6623 respectively). The trend of elements noted in the EDX was consistent with the phases formed in the XRD spectra (Fig. 17g).

4. Conclusions

Hybrid Al-6061 composites were developed by the blend of PKA, RHA, and waste steel debris (at a constant 4 wt % quantity) as reinforcement. The following are arrived at.

a) the microstructural features of the composites were noted to contribute significantly to the response parameters.
b) the analysis of variance revealed that PKA, RHA, and stirring temperature had significant contributions to all response parameters examined.
c) developed models for predicting each response is term statistically fit for response prediction.
d) increasing the proportion of PKA and RHA from 2 to 6% contributed to boosting yield and ultimate tensile strength and elastic modulus. As for impact strength, 2–6% resulted in a reduction in strength. 2–4% improved fracture toughness while 4–6% spawned a reduction in fracture toughness.
e) as for stirring temperature, 700 to 800 °C showed enhancement of yield, ultimate tensile, impact strengths, and elastic modulus while 800 to 900 °C is detrimental to the strength properties. A temperature value between 700 and 900 °C is detrimental to fracture toughness.

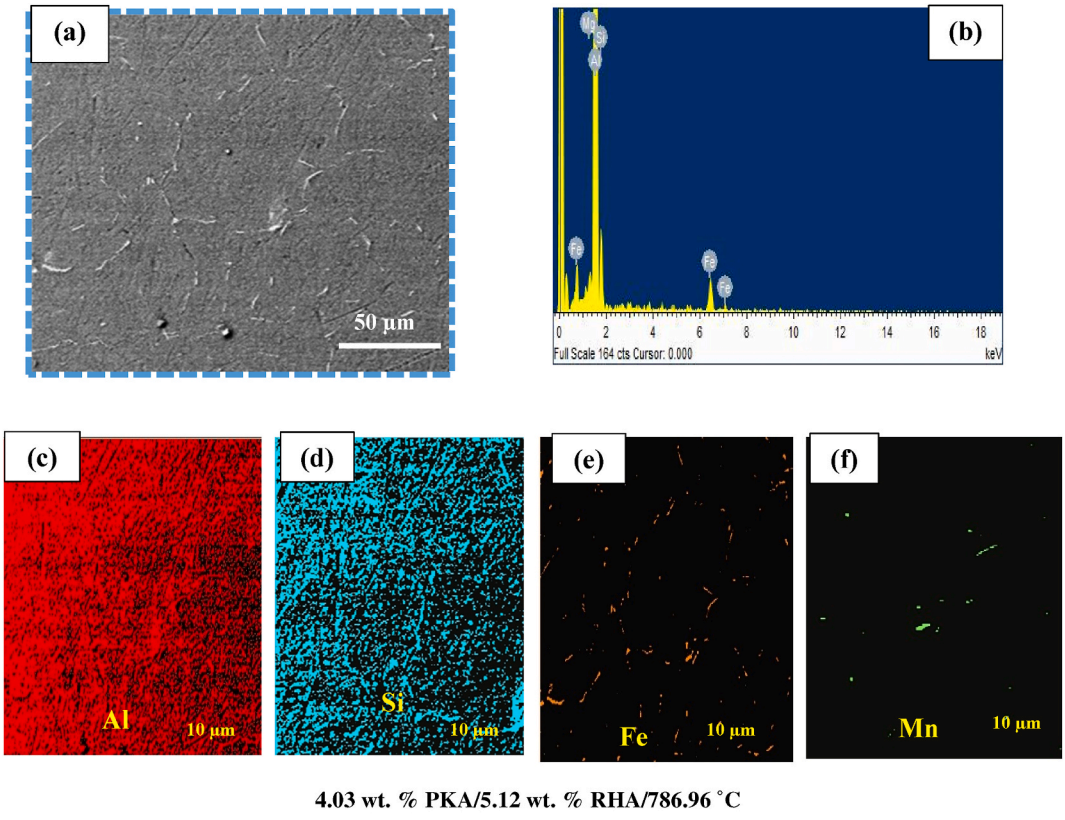

Fig. 17. Experimental results of the sample at optimal conditions showing (a) microstructure (b) EDX spectra (c–f) mapping for Al, Si, Fe and Mn respectively and (g) XRD spectra.

f) optimal condition obtained by the response surface method is 4.03095% PKA, 5.1207% RHA, and 786.957 °C stirring temperature. Prediction for the responses was 338.069 MPa for yield strength, 415.133 MPa for ultimate tensile strength, 34.0482 MPa $m^{0.5}$ for fracture toughness, 25.3134 J for impact strength, and 101.228 GPa for elastic modulus.

g) the validation experiment conducted at the optimum condition yielded 326.11 MPa, 402.64 MPa, 35.11 MPa $m^{0.5}$, 24.71 J, and 98.4 GPa for yield strength, UTS, fracture toughness, impact strength, and elastic modulus respectively. Since the error is <5%, the models are termed validated to be statistically fit for the prediction of response. It was concluded that 4.03095 wt% PKA, 5.1207 wt % RHA, and 4 wt % WSD at 786.957 °C stirring temperature is fit for the development of green-hybrid Al-6061 for automobile application.

Author contribution statement

Adeolu Adesoji Adediran - Conceived and designed the experiments; Analyzed and interpreted the data; Contributed reagents,

materials, analysis tools or data; Wrote the paper

Abayomi Adewale Akinwande - Analyzed and interpreted the data; Wrote the paper; Contributed reagents, materials, analysis tools or data.

Victor Agbaso - Performed the experiments; Analyzed and interpreted the data; Wrote the paper.

Adesina S. Olanrewaju; Oluwatosin Abiodun Balogun - Analyzed and interpreted the data; Wrote the paper.

B. Ravi Kumar - Contributed reagents, materials, analysis tools or data; Wrote the paper.

Funding

The authors did not receive financial support from any organization for the submitted work.

Data availability statement

No data was used for the research described in the article.

Additional information

No additional information is available for this paper.

Declaration of competing interest

The authors declare that they have no known competing financial interests or personal relationships that could have appeared to influence the work reported in this paper.

Acknowledgments

Adeolu Adesoji ADEDIRAN wishes to thank the Council of Scientific and Industrial Research (CSIR), India, and The World Academy of Sciences (TWAS), Italy, for the CSIR-TWAS Postdoctoral Fellowship (Award No.22/FF/CSIR-TWAS/2022) to pursue his Post-doctoral Fellowship program in CSIR-National Metallurgical Laboratory, Jamshedpur, India.

References

[1] A.A. Adediran, K.K. Alaneme, I.O. Oladele, E.T. Akinlabi, Processing and structural characterization of Si-based carbothermal derivatives of rice husk, Cogent Engineering 5 (1) (2018), 1494499.

[2] A.A. Akinwande, O.S. Adesina, A.A. Adediran, O.A. Balogun, D. Mukuro, O.P. Balogun, K.F. Tee, M.S. Kumar, Microstructure, process optimization, and strength response modeling of green-aluminium-6061 composite as automobile material, Ceramics 6 (1) (2023) 386–415, https://doi.org/10.3390/ceramics6010023.

[3] A.A. Adediran, A.A. Akinwande, O.A. Balogun, B.J. Olorunfemi, M.S. Kumar, Optimization studies of stir casting parameters and mechanical properties of TiO_2 reinforced Al 7075 composite using response surface methodology, Sci. Rep. 11 (1) (2021), 19860, https://doi.org/10.1038/s41598-021-99168-1.

[4] A.A. Akinwande, A.A. Adediran, O.A. Balogun, M.E. Yibowei, A.A. Barnabas, H.K. Talabi, B.J. Olorunfemi, Optimization of selected casting parameters on the mechanical behaviour of Al 6061/glass powder composites, Heliyon 8 (2022) (2022), e09350, https://doi.org/10.1016/j.heliyon.2022.e09350.

[5] A.A. Adediran, M. Sriariyanum, Applicability of agro-waste materials in the development of aluminium matrix composites for transport structures, Applied Science and Engineering Progress 16 (2) (2022) 6634, 6634.

[6] A.S. Kumar, A.A. Akinwande, C.H. Yang, V. Margabandu, V. Romanovski, Investigation on the Mechanical Behavior of Al-Mg-Si Alloy Hybridized with Calcined Eggshell and TiO_2 Particulates, Biomass Conversion and Biorefinery, 2023, https://doi.org/10.1007/s13399-023-04215-8.

[7] P. Mangalore, Akash, A. Ulvekar, Abhiram, J. Sanjay, Advaith, Mechanical properties of coconut shell ash reinforced aluminium metal matrix composite, AIP Conf. Proc. 2018 (20014) (2019) 1–7, https://doi.org/10.1063/1.5092897.

[8] L. Purushothaman, P. Balakrishnan, Wear and corrosion behavior of coconut shell ash (CSA) reinforced Al6061 metal matrix composite 62 (1) (2019) 77–84, https://doi.org/10.3139/120.111456.

[9] N.E. Udoye, O.S.I. Fayomi, A.O. Inegbenebor, Fractography and tensile properties of AA6061 Aluminium alloy/rice husk ash silicon nanocomposite, Int. J. Chem. Eng. 2020 (8818224) (2020) 1–8, https://doi.org/10.1155/2020/8818224.

[10] F.O. Edoziuno, C.C. Nwaeju, A.A. Adediran, B.U. Odoni, V.R.A. Prakash, Mechanical and microstructural characteristics of aluminium 6063 alloy/palm kernel shell composites for lightweight applications, Scientific African 12 (2021) (2021), e00781, https://doi.org/10.1016/j.sciaf.2021.e00781.

[11] U.S. Ikele, K.K. Alaneme, A. Oyetunji, Mechanical behaviour of stir-cast aluminum matrix composites reinforced with silicon carbide and palm kernel shell ash, Manuf. Rev. 9 (2022) 12.

[12] C.U. Atuanya, A.T. Esione, F.A. Anene, Effects of bamboo leaf stem ash on the microstructure and properties of cast Al-Si-Mg/bamboo leaf stem ash particulates composites, Journal of the Chinese Advanced Materials Society (2018), https://doi.org/10.1080/22243682.2018.1522276.

[13] P.K. Bannaravuri, A.K. Birru, Strengthening of mechanical and tribological properties of Al-4.5%Cu matrix alloy with the addition of bamboo leaf ash, Results Phys. 10 (2018) (2018) 360–373, https://doi.org/10.1016/j.rinp.2018.06.004.

[14] K.K. Alaneme, B.O. Ademilua, M.O. Bodunrin, Mechanical properties and corrosion behaviour of aluminium hybrid composites reinforced with silicon carbide and bamboo leaf ash, Tribology in Industry 35 (1) (2013) 25–35.

[15] S. Jannet, R. Raja, S.R. Ruban, S. Khosla, U. Sasikumar, N.B. Sai, P.J. Teja, Effect of eggshell powder on the mechanical and microstructure properties of AA 2024 metal matrix composite, Mater. Today: Proc. 44 (2021) 135–140, https://doi.org/10.1007/s41230-018-8105-3.

[16] A.A. Adediran, F.O. Edoziuno, O.S. Adesina, K.O. Sodeinde, A.B. Ogunkola, G.A. Oyinloye, C.C. Nwaeju, E.T. Akinlabi, Mechanical characterization and numerical optimization of aluminum matrix hybrid composite, Mater. Sci. Forum 1065 (2022) 47–57.

[17] O.A. Ogunsanya, A.A. Akinwande, R.M. Radhakrishnan, H.K. Talabi, M.S. Kumar, V. Margabandu, A. Bhownik, Experimental investigation on the mechanical performance of the Al_2O_3 and ZrO_2 added Al-Mg-Si alloy for structural applications, Journal of Process Mechanical Engineering (2023) 1989–1996, https://doi.org/10.1177/09544089231159777.

[18] B. Subramaniam, B. Natarajan, B. Kaliyaperumai, S.J.S. Chelladurai, Investigation on mechanical properties of aluminium 7075-boron carbide-coconut shell fly ash reinforced hybrid metal matrix composites, China Foundry 15 (6) (2018) 449–456, https://doi.org/10.1007/s41230-018-8105-3.

[19] R. Girimurugan, R. Pugazhenthi, T. Suresh, P. Maheskumar, M. Vairavel, Prediction of mechanical properties of hybrid aluminum composites, Mater. Today: Proc. (2020), https://doi.org/10.1016/j.matpr.2020.09.032.

[20] S. Arunkumar, A.S. Kumar, Studies of eggshell and SiC reinforced hybrid metal matrix composites for tribological application, Silicon 14 (2022) 1959–1967, https://doi.org/10.1007/s12633-021-00965-0.

[21] H.K. Talabi, A.M. Ojomo, O.E. Folorunso, J.F. Akinfolarin, J.P. Kumar, A.A. Akinwande, M.S. Kumar, Development of Hybrid Aluminium Alloy Composites Modified with Locally Sourced Environmental Wastes. Advances in Materials and Processing Technologies, 2022, https://doi.org/10.1080/2374068X.2022.2096831.

[22] K.K. Alaneme, A.V. Fajemisin, N.B. Maledi, Development of Al-based composites reinforced with steel and graphite particles: structural, mechanical and wear characterization, Journal of Material Research and Technology 8 (1) (2019) 670–682.

[23] K.K. Alaneme, C.A. Oganbule, A. Adewale, Circumferential notch test-based fracture toughness investigation of Al-Mg-Si alloy composites reinforced with alumina and quarry dust, Journal of Chemical Technology and Metallurgy 55 (2) (2019) 469–478.

[24] O.S. Adesina, A.A. Akinwande, O. Balogun, A.A. Adediran, O.O. Sanyaolu, V. Romanovski, Statistical analysis and optimization of the experimental results on the performance of green aluminium-7075 hybrid composites, Journal of Composite Science 7 (3) (2023) 115, https://doi.org/10.3390/jcs7030115.

[25] J. Zhang, Z. Kou, Y. Yang, B. Li, X. Li, M. Yi, Z. Han, Optimization of the heat treatment process for damping properties of Mg-13Gd-4Y-2Zn-0.5Zr Magnesium alloy using Box-Behnken design method, Metals 9 (2) (2019) 157, https://doi.org/10.3390/met9020157.

[26] O.S. Stamenkovic, M.D. Kostic, D.B. Radosavljevic, V.B. Veljkovic, Comparison of Box-Behnken, face central composite and full factorial designs in optimizing of hempseed oil extraction by n-hexane: a case study, Period. Polytech. - Chem. Eng. 1148 (2018) 1–9, https://doi.org/10.3311/PPch.11448.

[27] ASTM E8/E8M-21, Standard Test Methods for Tension Testing of Metallic Materials, ASTM International., West Conshohocken, PA, 2021.

[28] IS 1757 Part 1, Metallic Materials-Charpy Pendulum Impact Test Part 1, Test Method Indian Standard, New Delhi, India, 2020.

[29] M. Javanbakht, Phase evolution under hydrostatic pressure in a single imperfect crystal due to nanovoids, Materialia 20 (2021), 101199.

[30] ASTM D 3906-19, Standard Test Methods for Determination of Relative X-Ray Diffraction Intensities of Faujasite-type Zeolite-Containing Materials, ASTM International, West Conshohocken, PA, 2019.

[31] S.K. Dwiwedi, A.K. Srivastava, K.I. Sugimoto, M. Chopkar, Microstructural and mechanical characterization of chicken eggshell-reinforced Al6061 matrix composites, Open J. Met. 8 (2018) 1–13, https://doi.org/10.4236/ojmetal.2018.81001.

[32] P.E. Imoisili, K.O. Ukoba, T.C. Jen, Green technology extraction and characterization of silica nanoparticles from palm kernel shell ash via sol-gel, J. Mater. Res. Technol. 9 (1) (2020) 307–313, https://doi.org/10.1016/j.jmrt.2019.10.059.

[33] K.N. Farooque, M. Zaman, E. Halim, S. Islam, M. Hossain, Y.A. Mollah, A.J. Mahmood, Characterization and utilization of rice husk ash (RHA) from rice mills of Bangladesh, Bangladesh J. Sci. Ind. Res. 44 (2) (2009) 157–162, https://doi.org/10.3329/bjsir.v44i2.3666.

[34] A.F. Boostani, S. Tahamtan, Z.Y. Jian, D. Wei, S. Yazdani, R.A. Chosroshaki, R.T. Mousavian, J. Xu, X. Zhang, D. Gong, Enhanced tensile properties of aluminium matrix composites reinforced with graphene-encapsulated SiC nanoparticles, Composites Part A 68 (2015) (2015) 155–163, https://doi.org/10.1016/j.compositesa.2014.10.010.

[35] A.S. Negi, T. Shanmugasundaram, Hybrid particle dispersion strengthened aluminium metal matrix composite processed by stir casting, Mater. Today: Proc. (2020), https://doi.org/10.1016/j.matpr.2020.03.0717.

[36] S. Shin, H. Park, B. Park, S.B. Lee, S.K. Lee, Y. Kim, S. Chao, I. Jo, Dispersion mechanism and mechanical properties of SiC reinforcement in aluminium matrix composites through stir-and die-casting processes, Appl. Sci. 11 (952) (2021) 1–13, https://doi.org/10.3390/app11030952.

[37] A.K. Chaubey, S. Scudino, N.K. Mukhopadhyay, M.S. Khoshkhoo, B.K. Mishra, J. Eckert, Effect of particle dispersion on the mechanical behaviour of Al-based metal matrix composites reinforced with nanocrystalline Al-Ca intermetallics, J. Alloys Compd. 5365 (2012) 5134–5137, https://doi.org/10.1016/j.allcom.2011.12.075.

[38] S. Mozammil, P. Verma, J. Karloopia, P.K. Jha, Investigation and measurement of porosity in Al + 4.5Cu/6 wt. % TiB2 in-situ composites: optimization and statistical Modelling, J. Mater. Res. Technol. 9 (2020) 8041–8057, https://doi.org/10.1016/j.mrt.2020.05.045.

[39] J.A. Taylor, Iron-containing intermetallic phases in Al-Si-based casting alloys, Procedia Materials Science 1 (2012) (2012) 19–33, https://doi.org/10.1016/j.mspro.2012.06.004.

[40] B. Ling, H. Li, R. Xu, Y. Shi, H. Xiao, W. Zhang, K. Lu, Precipitation of iron-rich intermetallic and mechanical properties of Al-Si-Mg-Fe alloys with Al-5Ti-B, Mater. Sci. Technol. 34 (17) (2018) 1–8, https://doi.org/10.1080/02670836.2018.1519945.

[41] J. Matthew, G. Remy, M.A. Williams, F. Tang, P. Srirangam, Effect of Fe intermetallic on microstructure and properties of Al-Si alloys, J. Mater. 71 (12) (2019) 4362–4369, https://doi.org/10.1007/s11837-019-03444-5.

[42] A.A. Adediran, K.K. Alaneme, I.O. Oladele, E.T. Akinlabi, Microstructural characteristics and mechanical behaviour of aluminium matrix composites reinforced with Si-based refractory compounds derived from rice husk ash, Cogent Engineering 8 (1) (2021), 1897928, https://doi.org/10.1080/23311916.2021.1897928.

[43] J.C. Viala, M. Peronnet, F. Barbeau, F. Bosselet, J. Bouix, Interface chemistry in aluminium alloy castings reinforced with iron base inserts, Composites Part A 33 (2002) 1417–1420.

[44] O.S. Adesina, A.A. Akinwande, A.A. Adediran, O.A. Balogun, O.O. Sanyaolu, V. Romanovski, Morphological Evolution and Strength Performance of Green-Aluminium-7075 Hybrid Composites Modeled by Response Surface Analysis. Multiscale and Multidisciplinary Modeling, Experiments, and Design, 2023, https://doi.org/10.1007/s41939-023-00162-z.

[45] A.M. Roy, Influence of nanoscale parameters on solid–solid phase transformation in octogen crystal: multiple solution and temperature effect, JETP Lett. 113 (2021) 265–272, https://doi.org/10.1134/S0021364021040032.

[46] R. Anand Sekhar, R. Rakesh Pillai, M. Mubarak Ali, C.N. Shyam Kumar, Enhanced mechanical and wear properties of aluminium-based composites reinforced with a unique blend of granite particles and boron carbide for sustainable material recycling, J. Alloys Compd. (2023), https://doi.org/10.1016/j.jallocom.2023.171165.